A highly active and stable Ru catalyst for syngas production *via* glycerol dry reforming: Unraveling the interplay between support material and the active sites

Mert Ozden [a,1], Zafer Say [b,c,1], Yusuf Kocak [b], Kerem Emre Ercan [b], Ahsan Jalal [b], Emrah Ozensoy [b,d,*], Ahmet K. Avci [a,**]

[a] *Department of Chemical Engineering, Bogazici University, Bebek, 34342 Istanbul, Turkey*
[b] *Bilkent University, Department of Chemistry, 06800 Ankara, Turkey*
[c] *Department of Materials Science and Nanotechnology Engineering, TOBB University of Economics and Technology, 06510 Ankara, Turkey*
[d] *UNAM-National Nanotechnology Center, Bilkent University, 06800 Ankara, Turkey*

A B S T R A C T

Glycerol dry reforming (GDR) was studied on Ru/La$_2$O$_3$, Ru/ZrO$_2$, and Ru/La$_2$O$_3$–ZrO$_2$ catalysts. Impacts of the support on morphological, electronic and surface chemical properties of the catalysts were comprehensively characterized by TEM, *in–situ* DRIFTS, XPS, ATR–IR and XRD. Initial (5 h) CO$_2$ conversion at 750 °C and CO$_2$–to–glycerol ratio of 1–4 was ordered as Ru/La$_2$O$_3$ < Ru/ZrO$_2$ < Ru/La$_2$O$_3$–ZrO$_2$. During 72 h stability tests, Ru/ZrO$_2$ deactivated by ~33% due to Ru sintering, structural deformation of the monoclinic zirconia support, and strong metal–support interaction. Under identical conditions, CO$_2$ conversion on Ru/La$_2$O$_3$ decreased by 27% mainly due to dehydroxylation/carbonation of lanthana and severe coking. Lanthana–stabilized tetragonal zirconia phase of Ru/La$_2$O$_3$–ZrO$_2$ led to finely dispersed small oxidic Ru clusters which deactivated by 15% after 72 h and demonstrated unusually high catalytic performance that was on par with the significantly more expensive Rh–based catalysts, which are known with their exceptional activity and stability in GDR.

1. Introduction

Issues related with production and consumption of fossil fuels have accelerated efforts towards development of renewable fuels and their conversion processes. Biodiesel received notable interest as a renewable fuel as it can be blended with the refinery–based diesel without losing its compatibility with the current engines [1,2]. In biodiesel synthesis *via* transesterification of animal–based or vegetable oils, 1 mol of glycerol is obtained as a by-product for every 3 moles of biodiesel produced. This stoichiometry, however, causes an undesired build–up of glycerol as supply of glycerol is three times higher than its demand [3]. It is obvious that the method of handling excess glycerol dictates the cost of biodiesel production [4]. In this respect, its valorization into value–added products has become an active field of research [5]. Among several alternative routes, glycerol has been considered as a platform for producing hydrogen (H$_2$) and synthesis gas (syngas) at scales suitable for decentralized use.

Glycerol can be converted into syngas by steam reforming (SR), whose catalysis and reactor design aspects have been studied and reviewed extensively in the literature [6–8]. The resulting mixture is characterized by molar ratios of H$_2$/CO > 2, rendering SR suitable for H$_2$ production. However, syngas conversion processes, such as Fischer–Tropsch synthesis, require molar ratios of H$_2$/CO ~ 1 [9], which can be met conventionally by partial oxidation (POX) or autothermal reforming (ATR). Tuning the syngas composition in POX or ATR depends on the availability of pure oxygen or O$_2$-enriched air, both of which require expensive air separation units. Alternatively, syngas with molar ratios of H$_2$/CO ≤ 1 can be produced by reforming of glycerol with CO$_2$:

$$C_3H_8O_3 + CO_2 \rightleftharpoons 4CO + 3H_2 + H_2O \quad \Delta H° \quad = \quad 292 \text{ kJ/mol} \quad (1)$$
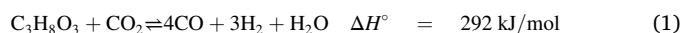
Provided that the heat demand of reaction (1) can be met without relying on fossil fuel utilization (*e.g., via* solar thermal reforming
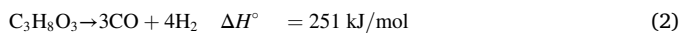
---

techniques [10]) GDR may offer a carbon–negative pathway. Reaction (1) can be envisioned as the combination of glycerol decomposition (2) and the reverse water–gas shift (RWGS, (3)) reactions [11]:

$$C_3H_8O_3 \rightarrow 3CO + 4H_2 \quad \Delta H° = 251 \text{ kJ/mol} \quad (2)$$

$$CO_2 + H_2 \rightleftharpoons CO + H_2O \quad \Delta H° = 41 \text{ kJ/mol} \quad (3)$$

Overall endothermicity of GDR necessitates temperatures in excess of 500 °C leading to thermal breakdown of glycerol to various species, such as methane, ethane, ethylene, acetaldehyde, acrolein, acetone, methanol, ethanol, and acetic acid [12]. These hydrocarbons and oxygenates can then be converted into surface carbon (C_s) species or coke as a function of catalyst and process parameters. Typical mechanisms of coke formation or gasification under the conditions of hydrocarbon reforming are presented in Table 1 [13]. It is also reported that carbon can form as pyrolytic, whisker-like or encapsulating type coke species depending on the operating conditions and the catalyst type [14]. While whisker and encapsulating carbon formation are observed on Ni–based catalysts, noble metal catalysts (*e.g.* Ru, Rh) do not dissolve carbon, *i.e.* do not favor whisker mechanism, and therefore are resistant against coking [15]. Under GDR conditions, it is possible to combat with coking by increasing the amount of inlet CO_2 to drive reverse Boudouard reaction (12). The same strategy also favors RWGS to produce steam that will gasify carbon *via* reactions (10) and (11). Coke formation is suppressed thermodynamically above 600 °C for inlet molar ratios of $CO_2/G > 1$ [12]. High temperatures also favor syngas production and increase CO production selectivity. For instance, increasing temperature from 600 to 750 °C also decreases the H_2/CO ratio from 1.17 to 0.86 [11]. Other possible side reactions that can occur at GDR conditions are shown in Table 1.

While the GDR literature is still scarce, the number of studies follows an increasing trend in the recent years as reviewed by Bac et al. [16]. Majority of these studies involved investigation of Ni–based catalysts primarily due to their inherently high activity in dry and steam reforming of hydrocarbons [9,16–18]. Monometallic (Ni/γ–Al$_2$O$_3$ [19], Ni/ZrO$_2$ [20], Ni/CaO [20], Ni/SBA–15 [21], Ni/CaO–SiO$_2$ [22,23], mesoporous Ni/MgO.Al$_2$O$_3$ [24] and bimetallic (La–Ni/Al$_2$O$_3$ [25–27], Ag–Ni/Al$_2$O$_3$ [28], Ag–Ni/SiO$_2$ [29], Re–Ni/CaO [20], Re–Ni/SBA–15 [21] catalysts were studied within 600–900 °C, with molar ratios of $CO_2/G = 0.5$–5 under atmospheric pressure, and at residence times between 1.4 and 7.2×10^4 ml/g$_{cat}$.h yielding glycerol conversion and H_2/CO molar ratios ranging between 3% and 100% and 0.5–2, respectively. Some of these former studies [22,25] also reported 72 h time––on–stream catalytic stability results which commonly indicated partial (*i.e.,* >25%) loss in glycerol conversion to gaseous products or complete deactivation of the Ni–based catalysts. In many of these studies, catalytic activity was reported only in terms of glycerol conversion to gaseous

products (namely, H_2, CH_4, C_2H_4, and C_2H_6) calculated by means of a mole balance on H. However, CO_2 conversion, which is a much more reliable metric for catalytic activity and stability due to its direct calculation from the measurement of consumed CO_2, was not mentioned in many of these former studies.

For the first time in the literature, both CO_2 and glycerol conversions were reported by Bulutoglu et al. [30] for two precious metal catalysts, namely 1 wt% Rh/ZrO$_2$ and 1 wt% Rh/CeO$_2$. Extensive structural characterization of these catalysts before and after the reaction within 600–750 °C, and $CO_2/G = 1$–4 clearly reveled the impact of the support on the activity and stability. It was shown that the average Rh nanoparticle size dispersed on ZrO$_2$ (~2 nm) was smaller than that of CeO$_2$ (~3.5 nm) rendering Rh/ZrO$_2$ catalyst more active than Rh/CeO$_2$, where the former catalyst revealed CO_2 and glycerol conversions up to 30% and 85%, respectively [30]. Nevertheless, stronger interaction of Rh with CeO$_2$ made the Rh/CeO$_2$ catalyst more stable (23% loss in CO_2 conversion) than Rh/ZrO$_2$, since Rh/ZrO$_2$ showed 40% loss in CO_2 conversion after 72 h stability tests due to combined effects of surface migration of Rh species and coke formation. Despite their deactivation, Rh–based catalysts remained more active and stable than their Ni–based counterparts. In a follow–up study by Bac et al. [31] significant improvements in the activity and stability of both Rh and Ni–based catalysts were demonstrated upon the use of Al$_2$O$_3$–ZrO$_2$–TiO$_2$ (AZT), a ternary oxide, as the support. After 72 h stability tests at 750 °C and by using a molar ratio of $CO_2/G = 4$, it was demonstrated that CO_2 conversions measured on ZrO$_2$– and CeO$_2$–supported Rh catalysts decreased by up to 40% [30], while only < 13% loss in CO_2 conversion was detected on 1 wt% Rh/AZT, and 5 wt% Ni/AZT catalysts [31]. At 750 °C, $CO_2/G = 2$–4, and 0.5 mg$_{cat}$.min/Nml, (*i.e.,* the shortest residence time investigated), Rh/AZT was capable of delivering CO_2 conversion up to 39%, which corresponded to > 90% of the pertinent thermodynamic limit [31]. A similar performance was observed on Ni/AZT at a residence time above 1.25 mg$_{cat}$.min/Nml. Stable nature of the AZT supported catalysts was also confirmed by comparative transmission electron microscopy (TEM), X-ray photoelectron spectroscopy (XPS), and X-ray absorption near edge spectroscopy (XANES) analyses of the samples before and after the GDR reaction [31]. GDR performances of noble metal catalysts were also studied by Tavanarad et al. [32] who prepared Rh, Ru, Ir, Pd, and Pt catalysts supported on MgAl$_2$O$_4$, and tested them within 600–750 °C, and $CO_2/G = 0$–3. Activity of these noble metals was reported to decrease in the following order: Rh > Ru > Ir > Pd > Pt. GDR catalytic performance tests of the noble metal catalysts commonly pointed out Rh as the most active metal yielding the highest activity and stability [30–32]. High performance of Rh, however, is often masked by its elevated cost that hinders its use. Ru is significantly cheaper than Rh (*i.e.,* current Rh price is >20 times higher than that of Ru [33]), while revealing only slightly lower or sometimes comparable hydrocarbon reforming activities to that of Rh [32,34]. Hence, Ru can be considered as a promising alternative for GDR. While Ru/MgAl$_2$O$_4$ catalyst has been investigated in a former report [32], detailed understanding of the influence of the support material on the catalytic performance is still mostly unknown. Thus, in the current work, we carried out extensive GDR activity/stability experiments accompanied by *in–situ/ex–situ* spectroscopic/imaging investigations on Ru active sites supported on ZrO$_2$, La$_2$O$_3$, and La$_2$O$_3$–ZrO$_2$ in an attempt to shed light on the structure–reactivity relationships. ZrO$_2$ supported catalysts are known to remain active in dry reforming reactions due to the presence of oxygen vacancies in ZrO$_2$ that promote dissociation of CO_2 into CO and O, where the latter species lead to the oxidation of surface carbon species [35–37]. Moreover, ZrO$_2$ promotes fine dispersion of Rh [30] and Ru [38] nanoparticles. Similar functional benefits that promoted catalytic activity and stability in biogas dry reforming set the basis for the consideration of La$_2$O$_3$–ZrO$_2$ as a promising mixed oxide support in the current work [39]. The notable impacts of the support material on metal dispersion, activity and stability were reported also for dry reforming of methane [40–44]. Along these lines, in

Table 1
Examples of various side reactions that can occur during GDR process.[a]

Reaction	$\Delta H°$ (kJ/mol)	Reaction Number
Dry reforming reactions		
$CH_4 + CO_2 \rightleftharpoons 2CO + 2H_2$	247	(4)
$C_2H_6 + 2CO_2 \rightleftharpoons 4CO + 3H_2$	430	(5)
$C_2H_4 + 2CO_2 \rightleftharpoons 4CO + 2H_2$	292	(6)
Steam reforming reactions		
$CH_4 + H_2O \rightleftharpoons CO + 3H_2$	206	(7)[a]
$C_2H_6 + 2H_2O \rightleftharpoons 2CO + 5H_2$	346	(8)[a]
$C_2H_4 + 2H_2O \rightleftharpoons 2CO + 4H_2$	210	(9)[a]
Surface carbon formation/gasification reactions		
$C_s + H_2O \rightleftharpoons CO + H_2$	131	(10)[a]
$C_s + 2H_2O \rightleftharpoons CO_2 + 2H_2$	90	(11)[a]
$C_s + CO_2 \rightleftharpoons 2CO$	172	(12)
$nC_s + (n + 1)H_2 \rightleftharpoons C_nH_{2n+2}$	< 0	(13)
$nC_s + nH_2 \rightleftharpoons C_nH_{2n}$	< 0	(14)

[a] Steam is not present in the feed mixture, but generated *via* RWGS reaction (3).

the current study, La_2O_3 was also investigated in benchmarking experiments to obtain insight regarding to its function in La_2O_3–ZrO_2 support material.

2. Experimental

2.1. Catalyst synthesis

1 wt% Ru/La_2O_3 (RuLa), 1 wt% Ru/ZrO_2 (RuZr), and 1 wt% Ru/La_2O_3–ZrO_2 (RuLZ) catalysts were synthesized by the incipient–to–wetness impregnation technique. Prior to impregnation, ZrO_2 (Alfa Aesar, >99% purity), La_2O_3 (Sigma Aldrich, 99.99% purity) and La_2O_3–ZrO_2 (Daiichi Kigenso Kagaku Kogyo, DKKK, Japan, 9 wt% La_2O_3) support materials were calcined at 800 °C in a muffle furnace under air for 4 h in an attempt to structurally stabilize these materials. Required amount (0.6 mL/g catalyst) of Ru precursor (ruthenium (III) nitrosyl nitrate solution, 1.5 wt% Ru, Sigma Aldrich) was dissolved in deionized water. The resulting solution was impregnated onto the thermally treated support materials by means of a peristaltic pump under vacuum for 90 min. This procedure yielded a slurry that was first dried overnight at 110 °C in air and then calcined at 800 °C in a muffle furnace in air for 4 h. Prior to the reaction tests, catalysts were pre––treated in–situ at 800 °C for 2 h under 40 Nml/min pure H_2 (purity > 99.99%, Linde GmbH) flow which was regulated by a Brooks 5850E Series mass flow controller (MFC). The fresh catalyst term used in the following sections refers to the state of the catalyst after the pretreatment protocol described above, which is followed by in–situ cooling under 30 Nml/min pure N_2 (purity > 99.99%, Linde GmbH) flow to room temperature, and transfer of the samples to airtight containers for post–characterization studies.

2.2. Catalytic activity and stability experiments

Catalytic performance tests were conducted in a down–flow, quartz, tubular packed bed reactor inserted in a three–zone furnace (Protherm PZF 12/50/500), whose geometric details were provided elsewhere [30]. Catalyst bed, which overlapped with the second zone of the furnace, consisted of a physical mixture of 10 mg of the calcined catalyst and 700 mg of inert diluent (α–Al_2O_3, Alfa Aesar). Catalyst bed was mechanically supported by a quartz wool plug. The resulting bed height (~1 ×10^{-2} m)–to–particle diameter (~2.8 ×10^{-4} m) and tube diameter (1 ×10^{-2} m)–to–particle diameter ratios of ~35 ensured minimization of diffusive transport effects and validity of plug flow profile, respectively without any pressure drop [45]. Research grade liquid glycerol (Sigma Aldrich, purity: 99.5%) was precisely dosed by a Shimadzu LC–20AD High Performance liquid chromatography (HPLC) pump to the quartz reactor tube via an externally heated 1/16 in. OD stainless steel line to give 4 Nml/min of glycerol vapor flow that was fixed in all experiments. Inlet flow of CO_2 (Linde GmbH, >99.99% purity) was adjusted according to the assigned CO_2/G ratio and inert N_2 (Linde GmbH, >99.99% purity) was used to make–up total inlet flow rate to 40 Nml/min. Flow rates of CO_2 and N_2 were controlled by Bronkhorst EL–FLOW Select MFCs.

Upon separation of the condensable species (i.e., H_2O, unreacted glycerol) by two serially connected cold traps, effluent gas stream was analyzed in two on–line gas chromatographs (GCs). The first GC, Shimadzu GC–2014, equipped with a 60–80 mesh size MS 5A packed column and a thermal conductivity detector (TCD) was used to quantify H_2, N_2, CH_4, and CO in Ar (Linde GmbH, > 99.99% purity, carrier gas) flow. The second GC, Shimadzu 8A was used to analyze CO_2 and C_1–C_2 hydrocarbons via a Porapak Q column–TCD configuration under He (Linde GmbH, > 99.99% purity) carrier gas flow. Sample injection was done via sampling valves integrated to each of the GC units. The GC analyzers ensured reproducible quantification of the CO, CO_2, N_2, H_2, CH_4, C_2H_4, and C_2H_6 species at ppm levels. Further details regarding evaporation, mixing, and injection of the feed mixture to the catalyst bed and

parameters of GC analysis were described elsewhere [30].

In the catalytic performance experiments run at atmospheric pressure, effects of CO_2/G ratio (1–4) and the residence time (0.25, 0.5 and 3.75 mg_{cat}.min/Nml, set by changing the mass of the catalyst) on reactant conversions and product yields were investigated. As justified comprehensively in our previous studies [30,31], temperature was fixed to 750 °C in all experiments. While studying the effect of a particular parameter, all other parameters were kept constant at their default values of CO_2/G = 3 and 0.25 mg_{cat}.min/Nml. Duration of the typical catalytic activity experiments was 5 h. After the onset of the reaction (i.e., "t_0") data were collected at every successive 45 min (except the very first data collected at t_0 + 30 min). Since the reaction reached a steady state after ~2 h of the initiation of the reaction, data acquired at t_0 + 30 and t_0 + 75 min were disregarded. In addition to the typical 5 h activity tests, 72 h stability experiments were also performed to follow the stability of the catalysts. These long–term stability tests were carried out at 3.75 mg_{cat}.min/Nml (corresponding to 150 mg of active catalyst without the diluent) for better monitoring of any deactivation phenomena due to the elongated contact of the reactive mixture with the catalyst. CO_2 conversion (x_{CO_2}) and product yield (Y_i), defined in Eqs. (15) and (16), respectively, were used as figures of merit to examine catalyst performance:

$$x_{CO_2}(\%) = \frac{F_{CO_2,in} - F_{CO_2,exit}}{F_{CO_2,in}} \times 100 \tag{15}$$

$$Y_i = \frac{F_{i,exit}}{F_{G,in}} \tag{16}$$

CO_2 conversion could be obtained from direct measurements of the inlet and exit CO_2 molar flow rates. However, this was not the case for the calculation of glycerol conversion using the difference between the glycerol contents in the inlet and the exit due to the complexities in the collection and quantification of the unreacted glycerol and H_2O from the cold traps. Therefore, in alignment with the GDR literature [16,46], glycerol conversion to gaseous products (x_G) was estimated from a mole balance on atomic H:

$$x_G(\%) = \frac{2F_{H_2,exit} + 4F_{CH_4,exit} + 4F_{C_2H_4,exit} + 6F_{C_2H_6,exit}}{8F_{G,in}} \times 100 \tag{17}$$

In Eqs. (15)–(17), $F_{i,in}$ and $F_{i,exit}$ (mol/min) are the molar flow rates of species i at the inlet and effluent, respectively. Eq. (17) accounts for the conversion of glycerol, the only inlet source of H, to detectable gaseous products, namely H_2, CH_4, C_2H_4, and C_2H_6. While it is commonly used in the GDR literature [16,46], x_G calculation using Eq. (17) does not provide useful insight regarding catalyst activity and stability due to the co–existence of significant non–catalytic glycerol breakdown [30,31] and the lack of H_2O in its formulation. Moreover, Eq. (17) includes both H_2 and C_1–C_2 hydrocarbons, indicators of high and low catalytic activity (Section 3.1), respectively. As a result, under the specified set of operating conditions, x_G values turn out to be almost equal for all catalysts and prevent differentiation of the catalyst performance [31]. Due to these concerns, in the current work, x_G is not used as a metric for quantifying catalytic response but still reported in Section 3.1 in order to draw comparison with the findings reported in the GDR literature. We also carried out mole balance calculations on atomic C, H and O (see Supporting Information (SI) for details) that allowed more realistic prediction of glycerol conversion and the molar amount of H_2O in the effluent stream. Outcomes of these calculations and their comparison with Eq. (17) were discussed in Section 3.1.

In order to quantify glycerol and possible CO_2 conversions in the absence of the catalyst, blank control experiments were conducted in a reactor packed only with inert α–Al_2O_3. Additional blank experiments involving calcined La_2O_3, ZrO_2 and La_2O_3–ZrO_2 support materials were carried out at 0.25 $mg_{support}$.min/Nml to examine the possible roles of individual supports on reactant conversions and product distribution. Fresh (pre–treated) and spent catalysts (after 72 h GDR reaction at

750 °C, $CO_2/G = 3$, residence time = 3.75 mg_{cat}.min/Nml) were characterized by transmission electron microscopy (TEM), X-ray photoelectron spectroscopy (XPS), *in–situ* diffuse reflectance infrared Fourier transform spectroscopy (DRIFTS), attenuated total reflection infrared (ATR–IR) spectroscopy, X-ray diffraction (XRD) and Brunauer–Emmett–Teller (BET) specific surface area analysis. Methodology used in these techniques are given in SI.

3. Results and discussion

3.1. Catalytic activity and stability measurements

3.1.1. Effect of feed composition

Conversion of CO_2 as a function of feed composition (*i.e.,* molar inlet CO_2/G ratio) for the investigated catalysts is presented in Fig. 1 which also includes equilibrium CO_2 conversions (*i.e.,* theoretical upper limits) computed using Gibbs Free Energy minimization technique *via* the ChemCad™ suite (v. 7.1.4). Methodology used in the thermodynamic calculations is given in SI.

Fig. 1a shows that x_{CO_2} was improved by increasing the relative inlet CO_2 concentration, and followed the order of RuLa < RuZr < RuLZ. The measured CO_2 conversions were intentionally kept at < 20% in all cases and remained well below the corresponding thermodynamic limits. These findings ensured that the observed responses under the currently used experimental conditions reflected the characteristics of the pertinent catalyst without any equilibrium restrictions. Additional experiments were run at $CO_2/G = 0$ (*i.e.,* only in the presence of glycerol) to quantify CO_2 production due to glycerol breakdown on the currently investigated catalysts. These results showed that catalytic glycerol decomposition to CO_2 was < ~7% by volume. Under typical reaction conditions utilized in the current work (*i.e.,* $CO_2/G = 1$–4), extensive amount of CO_2 present in the reaction feed is expected to thermodynamically suppress CO_2 formation *via* glycerol breakdown. Thus, we believe that Eq. (15) reflects actual consumption of CO_2 during GDR with reasonable accuracy.

The results in Fig. 1a can be further interpreted by analyzing the product yields presented in Fig. 1b–e. Enrichment of CO_2 in the feed led to a monotonic increase in CO yield along with a monotonic decrease in H_2 yield (Fig. 1b–e). These trends pointed out the impact of RWGS on product distribution and were coherent with the corresponding literature results on Rh, Ni and Co–based catalysts [30,31]. CO_2 was also consumed due to its reforming with CH_4, C_2H_4 and C_2H_6 *via* reactions (4–6), respectively, and reaction with C_s species *via* the reverse Boudouard reaction (12). *In–situ* generation of steam also contributed to the transformation of C_1–C_2 hydrocarbons to syngas *via* reactions (7–9), and to the gasification of C_s species *via* reaction (10). Extents of dry and steam reforming routes increased with the catalytic activity which also led to the suppression of the presence of C_1–C_2 hydrocarbons in the product mixture. While CH_4 yield on RuLa ranged between 5.3 and 5.7×10^{-1} mol/mol glycerol fed, it was lower (4.4–5.6 $\times 10^{-1}$ mol/mol

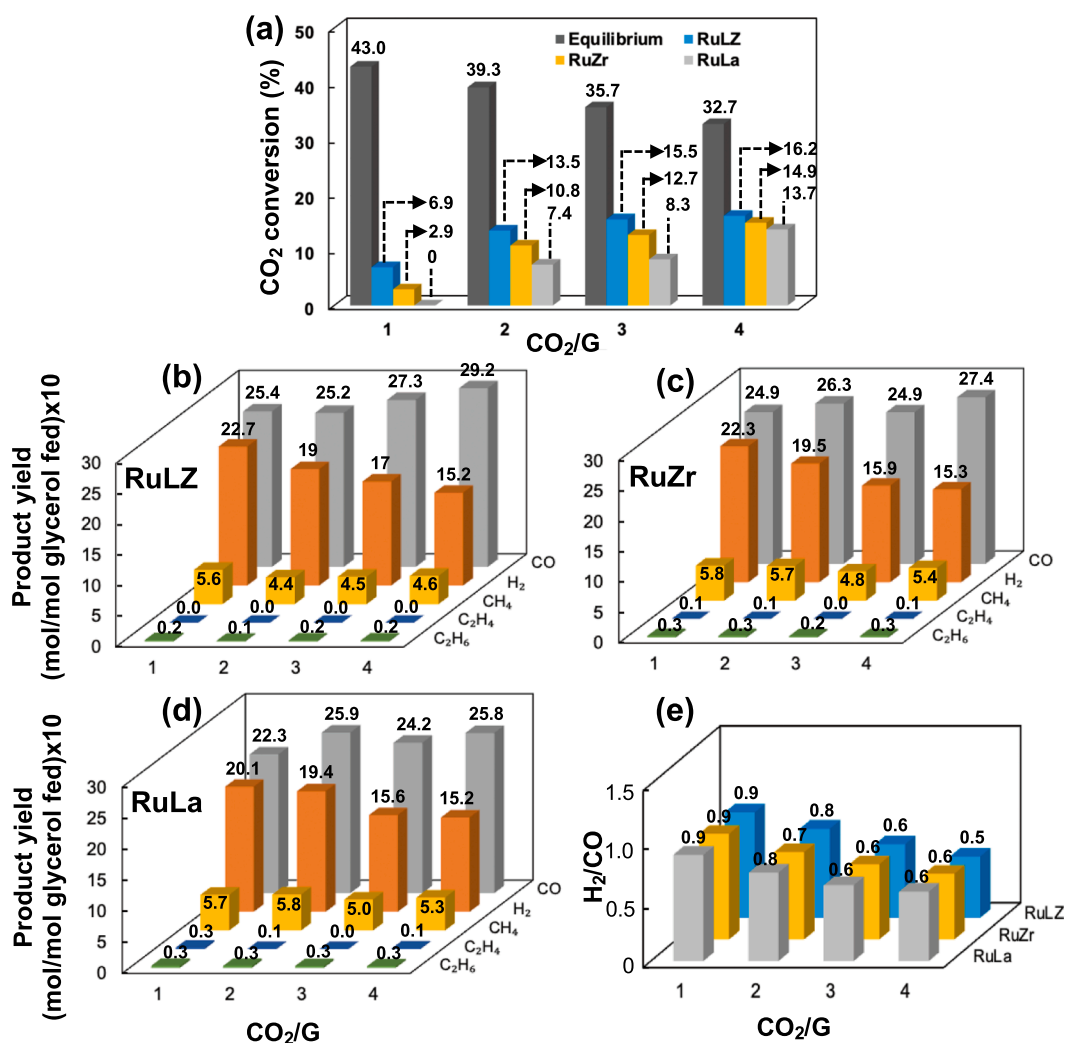**Fig. 1.** Effect of CO_2/G ratio on (a) CO_2 conversion for RuLZ, RuZr, and RuLa catalysts; product yields for (b) RuLZ, (c) RuZr, (d) RuLa catalysts, and (e) syngas composition in 5 h GDR reaction (T = 750 °C, residence time = 0.25 mg_{cat} min/Nml).

glycerol fed) on RuLZ (*i.e.,* the most active catalyst). Accordingly, average C_2H_6 yields were 3×10^{-2} and 2×10^{-2} mol/mol glycerol fed on RuLa and RuLZ, respectively. Moreover, C_2H_4 was not detected on RuLZ, whereas up to 3×10^{-2} mol C_2H_4 was produced per moles of glycerol fed on RuLa (Fig. 1b–d). In the absence of any catalysts, at 750 °C and $CO_2/G = 1$–4 (*i.e.,* for the entire range of currently investigated feed compositions), H_2 and CO yields were found to be ~5.8×10^{-1} and 12×10^{-1} mol/mol glycerol fed, respectively (not shown in Fig. 1b–d). These values were considerably lower than their catalytic counterparts reported in Fig. 1b–d and confirmed the predominantly catalytic nature of the syngas production pathways.

Experimental results given in Fig. 1 clearly illustrate the importance of the support in GDR. Fig. 1a shows that CO_2 conversion on RuLZ increased notably until $CO_2/G = 3$, above which the change in x_{CO_2} was limited to ~4%. In contrast, RuZr exhibited a monotonic increase in x_{CO_2} within $CO_2/G = 1$–4. For $CO_2/G = 3$–4, RuLa revealed a significant increase of ~65% in x_{CO_2} (Fig. 1a). As discussed in Section 3.2, the dissimilar catalytic behavior of RuLa can be attributed to the relative inefficiency of the surface carbon removal routes on this surface evident by the formation of relatively higher amounts of methane, ethane, and ethylene on RuLa as compared to RuLZ and RuZr (Fig. 1b–d) suggesting the hindrance of the catalytic steam/dry reforming of hydrocarbons to syngas on RuLa *via* reactions (4–9). In other words, increasing CO_2/G on RuLa facilities surface carbon removal and enhances x_{CO_2}. Activity measurements are in good alignment with current characterization results (Section 3.2) revealing typically higher concentrations of C_s species upon use of La_2O_3 as the support. It should be emphasized that presence of ZrO_2 in the support had a significant positive impact on x_{CO_2} and suppression of carbon deposition due to enhancement of Ru dispersion by ZrO_2 as validated by the current characterization studies (Section 3.2).

In contrast to CO_2 conversion, x_G values (estimated *via* Eq. (17)) were almost the same for all catalysts for a given feed composition. For example, at $CO_2/G = 1$, x_G ranged between 84% and 87%. Upon enriching the feed with CO_2 (*i.e.,* at $CO_2/G = 2$, 3, and 4), x_G progressively decreased to 71%, 66% and 62% on RuLZ; 79%, 66% and 67% on RuZr; and 80%, 66% and 67% on RuLa, respectively. These values were comparable with our previous findings on Rh, Ni and Co–based catalysts [30,31] and indicated that glycerol breakdown was somewhat independent from the support material. A reason of the similar glycerol conversion values under a given feed condition was the significant contribution of the non–catalytic breakdown of glycerol, which was quantified by blank experiments performed under identical operating conditions in a reactor containing only α–Al_2O_3. These results showed that ~39% of glycerol was converted to detectable gaseous species (*i.e.,* H_2, CH_4, C_2H_4, and C_2H_6) regardless of CO_2/G. These findings were also observed for blank experiments involving the support materials, all of which remained inert under current reaction conditions. Due to homogeneous conversion of glycerol, x_G was not used as a metric for catalytic activity in the current study. The x_G values based on Eq. (17), however, underestimated glycerol conversion due to the absence of H_2O that existed in the product stream. For this purpose, C, H and O mole balances were carried out in the context of the methodology explained in the SI. Outcomes of these calculations pointed out that, depending on the inlet CO_2/G ratio, glycerol conversions varied within 90–100% for RuLZ catalyst, and 88–100% for RuZr and RuLa catalysts. Glycerol conversions showed a decreasing trend upon CO_2 enrichment in the feed (SI, Table S3). These values were overestimated up to a maximum of 6% mainly due to the deviations in glycerol dosing to the reaction system (SI, Table S2). Note that the glycerol conversion values estimated by the equation (S.2) given in SI are typically greater than x_G calculated by Eq. (17) due to the lack of a H_2O–related term in the latter equation. Calculations showed that H_2O yield (mol/mol glycerol fed) was 0.6–1.2, 0.5–1.0 and 0.6–1.0 (with a maximum of 3% overestimation) on RuLZ, RuZr and RuLa catalysts, respectively. These values corresponded to molar H_2O fraction of ~7–13% in the GDR product stream (SI, Table S4)

and justified the underestimation of x_G predicted by Eq. (17). Positive correlation of the H_2O yields with CO_2/G (SI, Table S3) and the lack of H_2O formation in the experiments run without CO_2 in the feed suggested that RWGS reaction together with possible pathways of glycerol and/or intermediate species transformation in a CO_2–driven oxidative environment to H_2O–containing products were the possible reasons of H_2O formation under the current GDR conditions.

3.1.2. Effect of residence time

The effect of residence time on CO_2 conversion was investigated by adjusting the mass of the catalyst packed inside the reactor while keeping the total inlet flow rate constant. In this respect, 10, 20 and 150 mg of active catalyst, corresponding to residence times of 0.25, 0.5, and 3.75 mg_{cat}.min/Nml, respectively, were packed and tested at 750 °C, and $CO_2/G = 3$.

Effect of residence time on the CO_2 conversion values of the investigated catalysts is presented in Fig. 2. As expected, higher CO_2 conversions were observed when the residence time of the reactive mixture on the catalyst surfaces was increased. It can be seen in Fig. 2 that while RuLZ and RuZr converged to within 90% of the thermodynamic CO_2 conversion limit at 0.5 mg_{cat}.min/Nml (corresponding to a catalyst mass of 20 mg), RuLa was significantly far away from this equilibrium limit under these conditions. As will be further discussed in Section 3.2, this observation is consistent with the availability of a greater number of Ru active sites and the presence of a higher Ru dispersion on RuLZ and RuZr catalysts as compared to those of the RuLa catalyst. Due to the relatively smaller number of available Ru active sites on RuLa, this particular catalyst could approach equilibrium only at much higher residence times such as 3.75 mg_{cat}.min/Nml (*i.e.,* corresponding to a catalyst mass of 150 mg).

3.1.3. Stability of the catalysts

Stability of the catalysts under GDR reaction conditions was evaluated through 72 h stability experiments carried out at 750 °C and $CO_2/G = 3$ (Fig. 3). In these experiments, the residence time was set to the highest value used in the current work (*i.e.,* 3.75 mg_{cat}.min/Nml) in order to magnify the impacts of deactivation by increasing the interaction between the reactant mixture and the catalyst surface. Relative long–term activities of the catalysts, quantified in terms of x_{CO_2}, yields of H_2 and CO, of C_1+C_2 hydrocarbons are depicted in Fig. 3a–c. As can be clearly seen in Fig. 3a, all catalysts delivered initial CO_2 conversions close to the equilibrium value of 35.7% revealing only minor variations in activity. On the other hand, catalytic activity trends changed over extended durations of the GDR reaction. While RuLZ catalyst was able to preserve most of its initial catalytic activity at the end of the stability test, RuZr and RuLa catalysts lost significant extents of their initial activities after 72 h. Numerically, RuLZ catalyst could deliver 29.3% CO_2 conversion at the end of the stability test corresponding to 82% of the
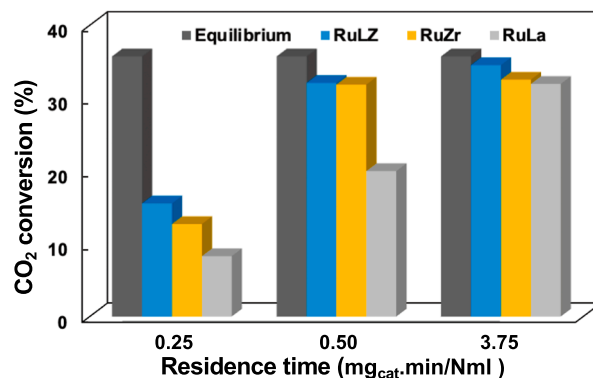

Fig. 2. CO_2 conversions obtained as a function of residence time (T = 750 °C, $CO_2/G = 3$).
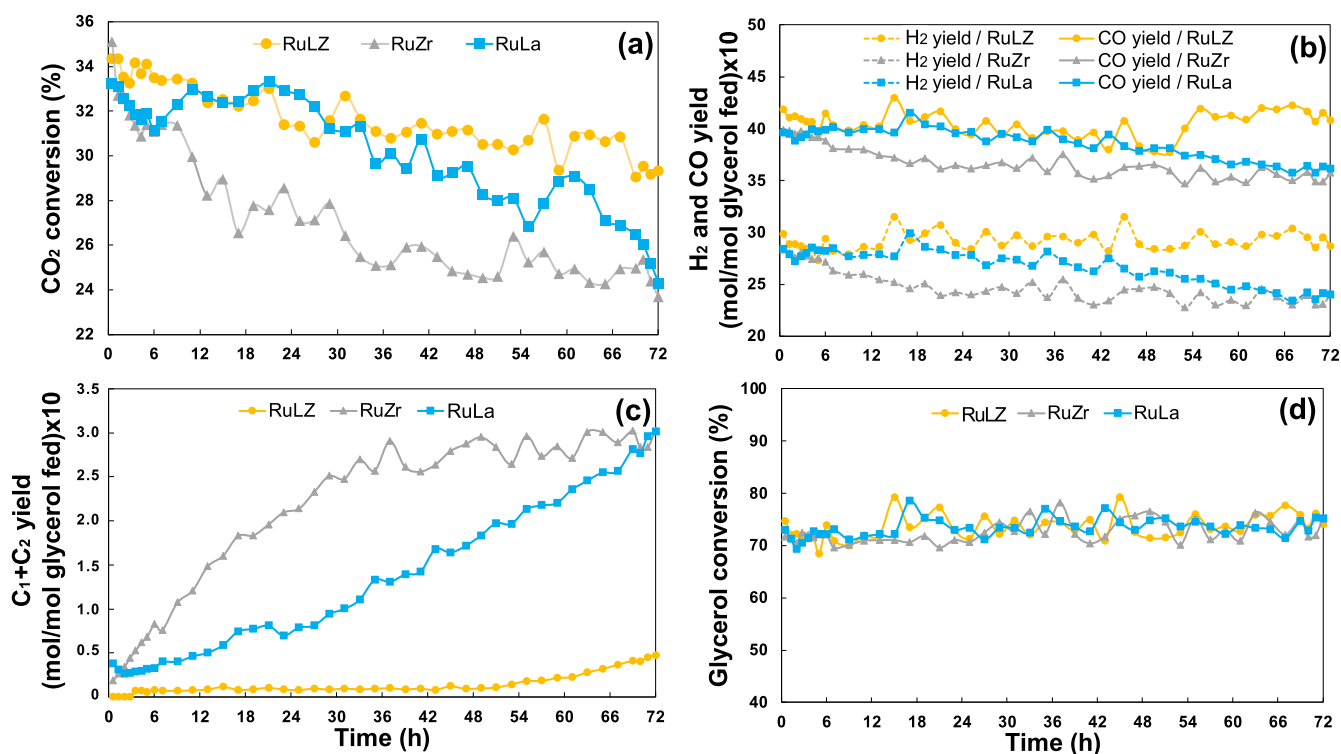
Fig. 3. (a) CO_2 conversions, (b) H_2 and CO yields, (c) sum of the yields of CH_4, C_2H_4 and C_2H_6, and (d) glycerol conversions in the 72 h stability testing of RuLZ, RuZr and RuLa catalysts (T = 750 °C, CO_2/G = 3, residence time = 3.75 mg_{cat} min/Nml).

pertinent equilibrium CO_2 conversion value under these reaction conditions. Note that the performance of RuLZ at the end of the 72 h catalytic stability test was close to that of a much more expensive Rh–based catalyst (1% Rh/Al_2O_3–ZrO_2–TiO_2) revealing 27.7% of CO_2 conversion at the end of a 72 h GDR test (carried out at T = 750 °C, CO_2/G = 4, residence time = 3.75 mg_{cat}.min/Nml) [31]. It is important to mention that while the ultimate CO_2 conversion values of RuLa and RuZr catalysts were similar (*i.e.,* x_{CO_2} = ~24%) at the end of the 72 h catalytic stability test, deactivation profiles of these two catalyst were quite dissimilar. Accordingly, RuLa catalyst was able to retain a large extent of its initial catalytic activity within the first 30 h of the stability test followed by a marked decrease in activity, whereas RuZr indicated a significant loss in activity even after the first 18 h of the stability test. Instability induced by the use of ZrO_2 as the support for GDR catalysis was also observed in a former study on 1% Rh/ZrO_2 catalyst, which was reported to lose 40% of its initial activity after 72 h stability test conducted at 750 °C and CO_2/G= 4 due to the combined effects of hydrothermal sintering and formation of C_s species [30].

Changes in the product yields as a function of time are presented in Fig. 3b and c. It is observed that the yields of H_2 and CO followed the order of RuLZ > RuLa > RuZr (Fig. 3b), whereas the opposite of this order dictated the C_1+C_2 yield trends (Fig. 3c) along the entire span of 72 h. These findings were well aligned with the CO_2 conversion data provided in Fig. 3a. In accordance with the previous reports [16,30,31], existence of CH_4, C_2H_4 and C_2H_6 in the product mixture is an indicator for lower catalytic activity. RuLZ seems to transform C_1–C_2 species into syngas primarily *via* catalytic steam and dry reforming routes, as evident from the limited yield of ~5 × 10^{-2} mol (C_1+C_2)/mol glycerol fed at the end of 72 h. However, under the same conditions, both RuZr and RuLa yield up to ~6 times more hydrocarbons (Fig. 3c). While the increase in the amount of C_1–C_2 species with time was almost linear on RuLa, a much sharper ramp was noted on RuZr. These findings can be attributed to the differences in the deactivation mechanisms of the catalysts comprehensively discussed in Section 3.2. Decrease in the syngas (H_2+CO) yield at the end of 72 h was not as significant as observed in

CO_2 conversion (Fig. 3a, b). Moreover, H_2 and CO yields on RuLZ remained almost unchanged with time. Reduced dependence of syngas formation on the type of support material can be attributed to glycerol conversion which remains clustered between ~72–74% for all catalysts in the entire range of stability tests (Fig. 3d) and confirms the contribution of non–catalytic glycerol breakdown discussed in Section 3.1.1. In this respect, homogeneous glycerol decomposition (Reaction 2) [16, 47] could be considered as a route that supplies H_2 and CO and dampens catalyst deactivation–driven effects causing decrease in syngas formation.

3.2. Structural and functional characterization studies

3.2.1. Analysis of specific surface area, Ru particle size, and coking of Ru active sites

BET analyses revealed specific surface area (SSA) values of 6, 33, and 58 m^2/g for La_2O_3, ZrO_2, and La_2O_3–ZrO_2 support materials, and 7, 27, and 46 m^2/g for the 1 wt% Ru loaded versions of these materials respectively. As will be demonstrated *via* current TEM data, higher SSA values of the currently investigated support materials typically led to smaller Ru particle sizes and enhanced distribution of Ru particles on the support surface.

Variation of Ru particle size and the distribution of Ru active sites on the La_2O_3–ZrO_2, ZrO_2, and La_2O_3 support materials were investigated *via* TEM imaging (Figs. 4–6) before and after 72 h catalytic stability tests. TEM images of the fresh RuLZ catalyst given in Fig. 4a, b (as well as numerous additionally acquired images not shown here) did not yield any clearly visible Ru nanoparticles suggesting the presence of extremely small Ru particles/clusters with diameters of < 1 nm which were finely dispersed on the LZ support surface and thus not detectable by the currently used TEM. This was also mostly the case for the spent RuLZ catalyst investigated after 72 h catalytic stability test (Fig. 4c, d) indicating the overall resilience of RuLZ catalyst against aging and particle size growth. Apparently, relatively higher SSA of the La_2O_3–ZrO_2 support material as compared to that of ZrO_2, and La_2O_3
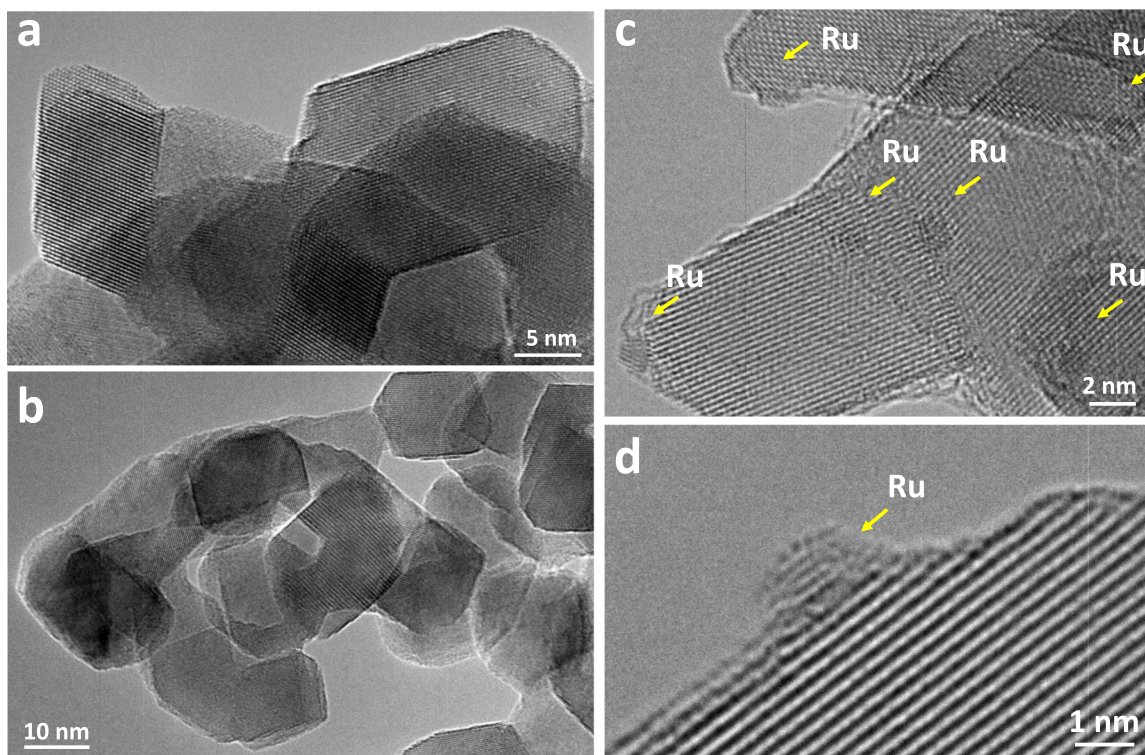
Fig. 4. TEM images of fresh (a and b) and spent (c and d) RuLZ catalyst after 72 h stability test carried out at T = 750 °C, CO_2/G = 3, residence time = 3.75 mg_{cat} min/Nml.
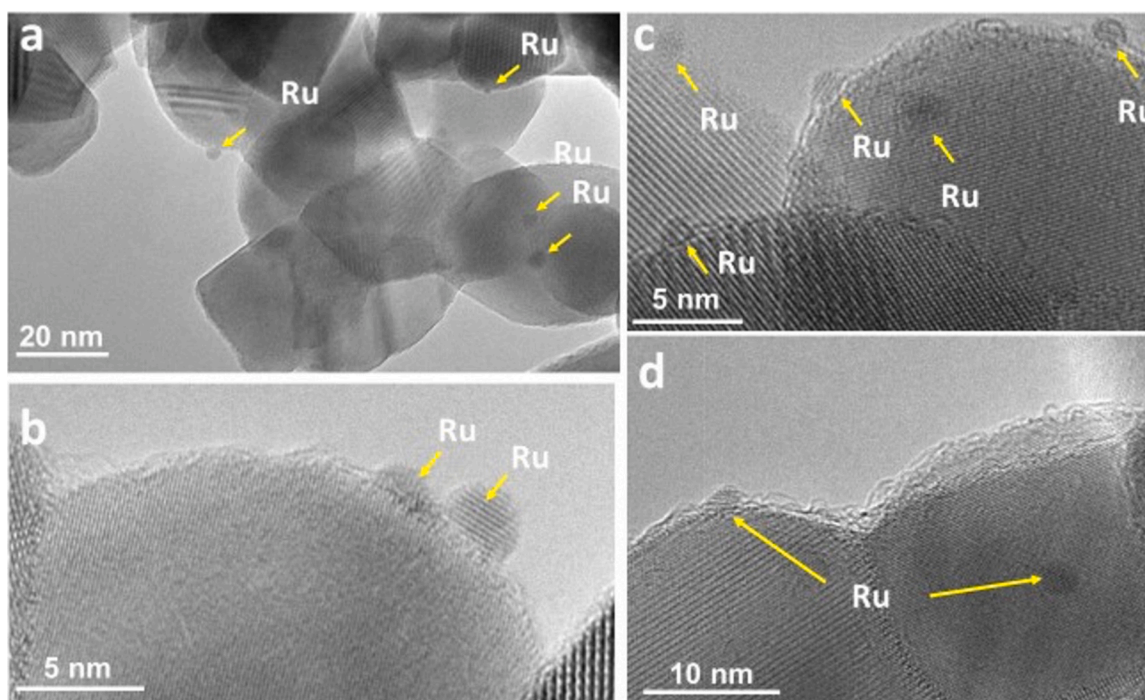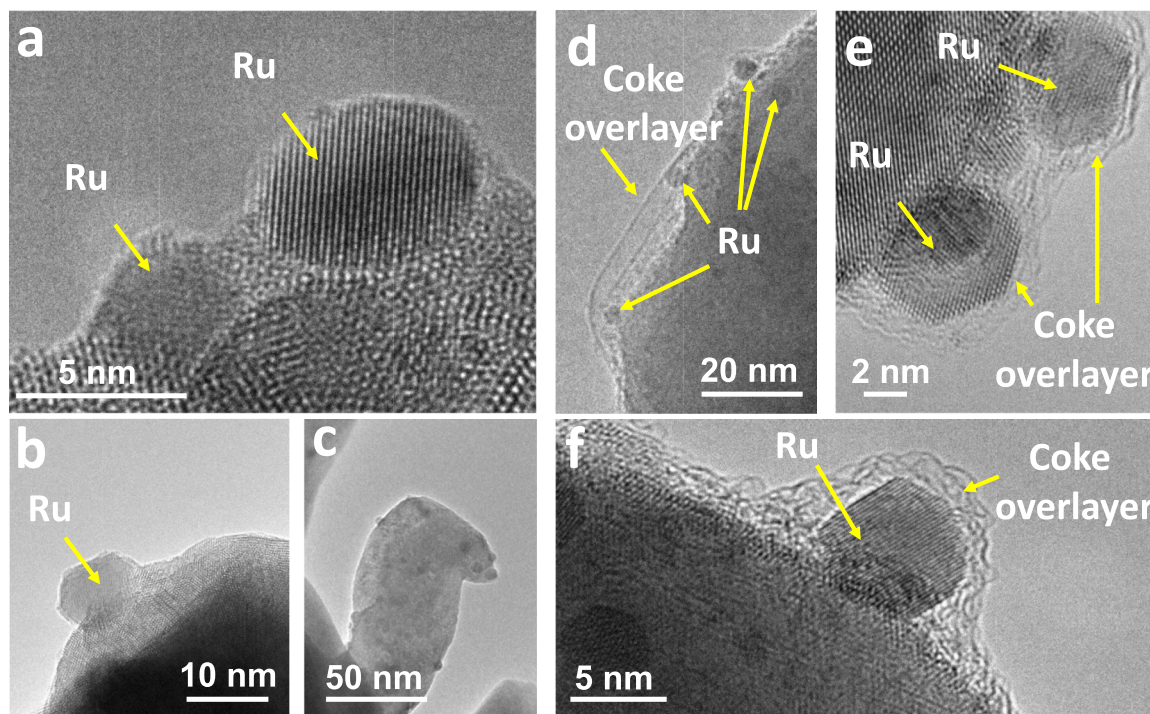

Fig. 5. TEM images of fresh (a and b) and spent (c and d) RuZr catalyst after 72 h stability test carried out at T = 750 °C, CO_2/G = 3, residence time = 3.75 mg_{cat} min/Nml.

enhanced the Ru distribution by offering a smaller average Ru particle size. However, a very small number of Ru particles exhibiting diameters within 1–2 nm was also present on the spent RuLZ catalyst (Fig. 4c, d) indicating a limited but detectable extent of sintering, probably due to an Ostwald ripening type of thermal aging mechanisms [48,49]. It is also

worth mentioning that TEM images of the spent RuLZ surface (Fig. 4c, d) revealed only minor signatures of coke overlayer formation.

Similar to the RuLZ catalyst, TEM analysis of the fresh (Fig. 5a, b) and spent (Fig. 5c, d) RuZr catalysts indicated the predominant presence of small Ru clusters with particle diameters of less than 1 nm that are

Fig. 6. TEM images of fresh (a–c) and spent (d–f) RuLa catalyst after 72 h stability test carried out at T = 750 °C, CO_2/G = 3, residence time = 3.75 mg_{cat} min/Nml.

below the spatial resolution of the currently used TEM. In addition, scarcely existing bigger Ru nanoparticles with diameters ranging within 2–3 nm were visible both on the fresh and spent RuZr catalyst. This latter observation presumably suggests the presence of typically larger Ru particles on the RuZr catalyst as compared to that of RuLZ in line with the lower SSA of the former catalyst. Furthermore, spent RuZr catalyst also showed similar characteristics of carbon deposition to that of the RuLZ catalyst. Since the coking on the spent RuLZ and spent RuZr catalysts was rather minor (which is also justified by the current XPS surface elemental composition results presented in Section 3.2.2), significantly faster and severe deactivation of the RuZr catalyst as compared to that of RuLZ (Fig. 3) can be associated with the bigger Ru particle size for the RuZr catalyst and variations in the nature of the strong metal support interactions (SMSI) between Ru sites and the corresponding support surfaces [50–52].

In stark contrast to RuLZ and RuZr catalysts, TEM images of the fresh (Fig. 6a–c) and spent (Fig. 6d–f) RuLa catalysts revealed readily visible and significantly larger Ru nanoparticles with diameters ranging between 5 and 8 nm. Note that, as in the case of RuLZ and RuZr catalysts, the presence of smaller Ru clusters with diameters of less than 1 nm on the fresh and spent RuLa catalysts cannot be ruled out. This argument is particularly supported by the current XRD data for fresh/spent RuLZ, RuZr, and RuLa catalysts given in Section 3.2.3 which lacked any detectable diffraction signals associated with metallic or oxidic Ru phases, despite relatively high nominal Ru loading (*i.e.*, 1 wt%) used in the catalyst synthesis. Another striking aspect of the spent RuLa catalyst is the drastic accumulation of the coke overlayer on the Ru nanoparticles after 72 h stability tests (Fig. 6d–f). Thus, significant deactivation of the RuLa catalyst after the first 30 h of the stability test (Fig. 3) can be ascribed to the increasing levels of coke deposition on Ru.

Average Ru–nanoparticle diameter as a function of the support material was also investigated *via* CO chemisorption studies presented in the SI section D. In alignment with the current TEM data and the SSA of the support materials, average diameter of the Ru–nanoparticles were found to increase in the following order: RuLZ (1.9 nm) < RuZr (4.1 nm) < RuLa (13.3 nm). Improved Ru–dispersions (Table S1, SI section D) on the Zr-containing support materials (*i.e.*, LZ and Zr) were found to be

coherent with the corresponding GDR activities of RuLZ and RuZr catalysts, which surpassed that of the RuLa catalyst (Figs. 1–2).

3.2.2. Surface elemental composition determination via XPS

Fig. 7 presents the corresponding C, Zr, and La surface atomic composition data for fresh and spent RuLZ, RuZr, and RuLa catalysts. The results show that both of the fresh RuLZ and RuZr catalysts exhibited relatively similar surface Zr atomic concentrations. This is not surprising since, as mentioned in the experimental section, the nominal La_2O_3 content of the LaZr support material was only 9 wt%. Another valuable information obtained from the XPS analysis given in Fig. 7 was the relative increase in the surface carbon content of the RuLZ, RuZr, and RuLa catalysts before and after the 72 h stability tests. Although initial surface carbon contents of the fresh RuLZ, RuZr, and RuLa catalysts were comparable, coking on RuLa was found to increase by a factor of 3.2 after the 72 h test. In contrast, corresponding increase in the coking on RuLZ and RuZr catalysts after the 72 h stability tests were comparably lower (*i.e.*, a factor of 2.3 and 1.5, respectively). Thus, it is
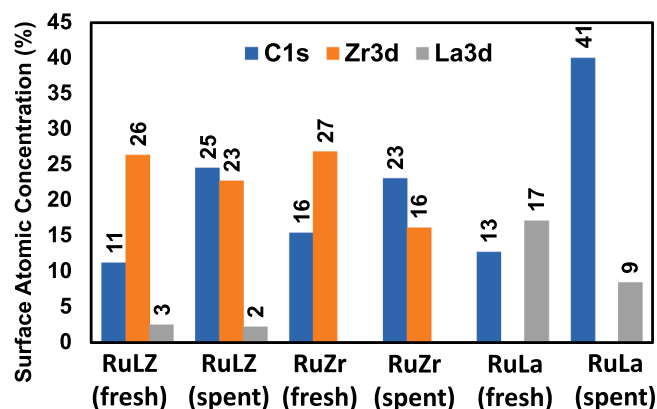
Fig. 7. Percent surface atomic concentration values obtained *via* XPS analysis of the fresh and spent (*i.e.*, after 72 h stability test carried out at 750 °C, CO_2/G = 3, residence time = 3.75 mg_{cat} min/Nml) RuLZ, RuZr, and RuLa catalysts.

evident that the extent of coking on RuLa under GDR conditions was much more drastic than those of RuLZ and RuZr. This finding is also in very good agreement with coke overlayers observed on the Ru particles in TEM images of the spent RuLa (Fig. 6d–f) catalysts as well as the corresponding ATR–IR spectroscopic results which will be presented in the forthcoming sections. Note that due to the well–known strong overlap between C1s and Ru3d XPS signals, analogous data for the determination of the surface atomic percentage of Ru atoms existing with much lower relative content (*i.e.*, 1 wt%) than C was not reported in the text. Likewise, determination of the accurate oxidation states of Ru species *via* XPS could not be accomplished. For additional information and the corresponding Ru3d and C1s XPS spectra, reader is referred to the SI (Fig. S1). Thus, in order to obtain information on the Ru oxidation states, we utilized CO as a probe molecule in the *in–situ* DRIFTS spectroscopic experiments.

3.2.3. Crystal structure analysis via XRD

XRD data given in Fig. 8 for fresh and spent forms of RuLZ, RuZr, and RuLa catalysts revealed no significant indications of crystalline Ru (ICDD card no: 00-006-0663) or RuO_2 (ICDD card no: 00-040-1290) phases, in line with the TEM data presented in Figs. 4–6) suggesting the lack of significant extents of Ru nanoparticles with diameters greater than 1 nm. In other words, XRD data shown in Fig. 8 is consistent with the fact that Ru sites were dispersed finely on the La_2O_3–ZrO_2, ZrO_2, and La_2O_3 support materials leading to predominantly small Ru clusters.

Furthermore, Fig. 8a indicates that fresh/spent RuLZ catalysts revealed strong diffraction signals associated with only tetragonal zirconia (ICDD card no: 00–042–1164) and lacked any XRD signals for any La–containing phases. In contrast, fresh and spent RuZr catalysts exhibited intense XRD signals that can be ascribed to a monoclinic zirconia phase (ICDD card no: 00-007-0343). Note that while current ATR–IR spectroscopic data (Figs. 9 and 10) indicates weak and convoluted signals for the possible existence of both tetragonal and monoclinic zirconia on RuLZ and RuZr, based on the strong XRD features given in Fig. 8a and b, it is likely that tetragonal zirconia is the dominant phase on RuLZ and the monoclinic zirconia is the prominent phase on RuZr. Considering the higher catalytic activity (Figs. 1 and 2) and the superior stability (Fig. 3) of the RuLZ catalyst as compared to that of RuZr and RuLa, it can be argued that lanthana–promoted tetragonal zirconia

phase present in the LZ support yielded a unique and a favorable SMSI with Ru active sites.

Fig. 8c shows that the fresh RuLa catalyst exhibited diffraction features corresponding to La_2O_3 (ICDD card no: 00-005-0602) and $La(OH)_3$ (ICDD card no: 01-075-1900) phases. After 72 h stability test, these phases transformed into lanthanum dioxycarbonate (*i.e.*, $La_2O_2(CO_3)$, ICDD card no: 04-009-3944) on the spent RuLa catalyst indicating dehydroxylation and carbonation of the RuLa support material. Thus, it is apparent that the deactivation route of the RuLa catalyst (Fig. 3) not only included severe coking as evident by the current TEM (Fig. 6) and XPS (Fig. 7) data but also involved a crystallographic modification of the RuLa support material. These findings were in very good agreement with the current ATR–IR results (Fig. 9), revealing significantly higher and different nature of carbon–content on RuLa catalyst after 72 h stability testing as compared to those of RuLZ and RuZr catalysts.

3.2.4. Identification of different types of carbonaceous species present in the catalyst coke deposits after GDR reaction via ATR–IR measurements

As illustrated in Fig. 9a, carbon–based deposits on RuLa yielded intense vibrational features at 1504, 1455, 1085, 854, and 744 cm^{-1}. Note that ATR–IR intensities of the vibrational features for RuLa were almost two orders of magnitude greater than that of RuLZ and RuZr catalysts (Fig. 9b) indicating stronger coking on RuLa, as evident from the higher degree of deactivation on this catalyst. Characteristic spectral line shapes of the 1504, 1455, 1085, and 854 cm^{-1} features observed for RuLa (Fig. 9a) were in accordance with the existence of amorphous carbonate nano-particulates [53–55]. Furthermore, ATR–IR signal located at 744 cm^{-1} could be assigned to crystalline carbonate phases formed on La_2O_3 [56–58] which is consistent with the observation of an ordered lanthanum dioxycarbonate (*i.e.*, $La_2O_2(CO_3)$) phase in the current XRD data (Fig. 8c). Presence of such species was also reported in former studies using *in–situ* time–resolved Energy Dispersive X-ray Diffraction (ED-XRD) and high–resolution electron microscopy [53,59].

Spectral line shapes and ATR–IR intensities of carbonaceous species on RuZr and RuLZ (Fig. 9b) were noticeably different than that of RuLa (Fig. 9a), suggesting significant differences in the nature and quantity of the carbonaceous deposits formed during the 72 h stability test. Fig. 9b showed that five major vibrational bands at 1567, 1428, 1224, 1125, and 1052 cm^{-1} were observed on RuZr and RuLZ. Among these features,
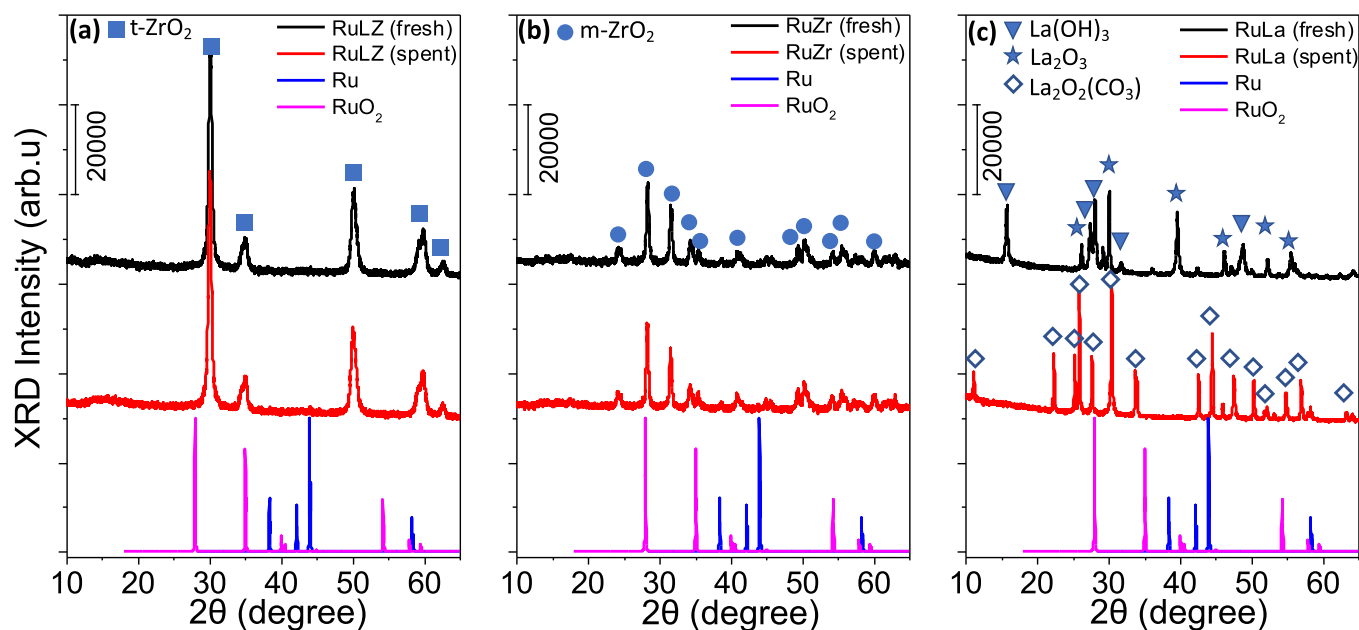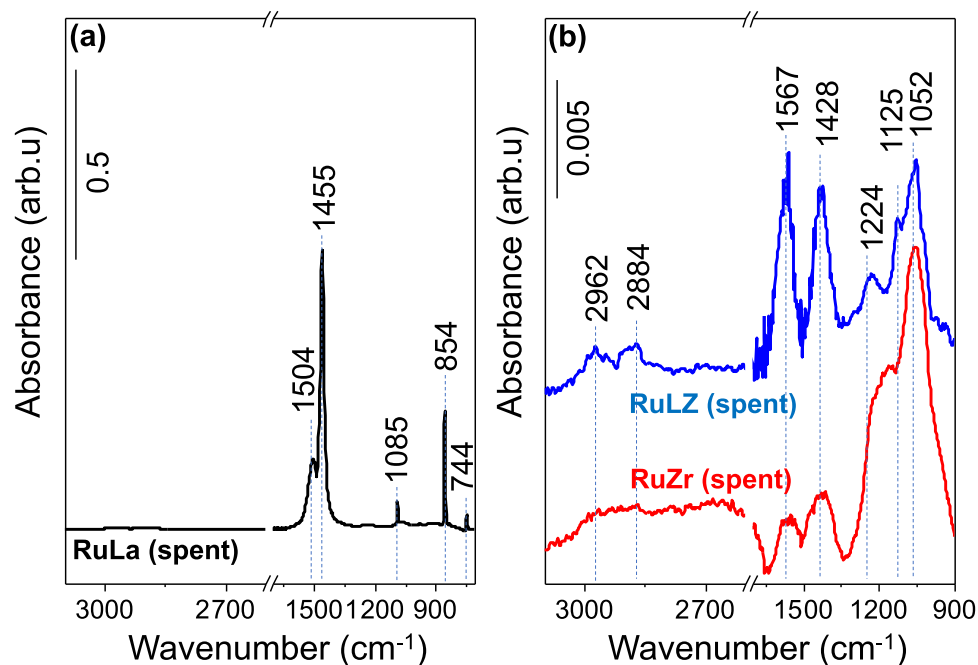

Fig. 8. XRD patterns corresponding to (a) RuLZ, (b) RuZr, and (c) RuLa catalysts before (fresh) and after (spent) 72 h stability tests carried out at 750 °C, $CO_2/G = 3$, residence time = 3.75 mg_{cat} min/Nml.

Fig. 9. Carbon deposit analysis of spent (a) RuLa, (b) RuLZ and RuZr catalysts after 72 h stability tests (T = 750 °C, CO₂/G = 3, residence time = 3.75 mg_cat min/Nml) *via* ATR–IR spectroscopy. Background spectra were acquired using the fresh forms of the pertinent catalysts.
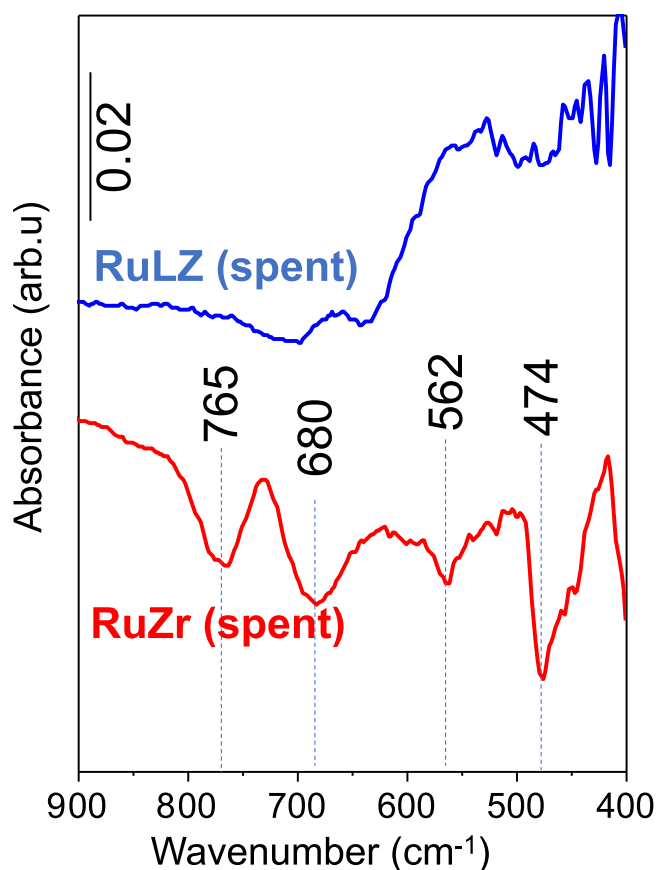
Fig. 10. ATR–IR spectra for the spent RuLZ and RuZr catalysts after 72 h stability tests (T = 750 °C, CO₂/G = 3, residence time = 3.75 mg_cat min/Nml) where fresh forms of the corresponding catalysts were used in the background spectra acquisition.

bands at 1567 and 1428 cm^{-1} can be ascribed to asymmetric and

symmetric O–C–O stretching vibrations of adsorbed formate species in accordance with a former CO_2 hydrogenation study on Rh/Al_2O_3 [60]. Similar vibrational features were also observed on Ru/Al_2O_3 *via in–situ* FTIR analysis during WGS reaction, and was further confirmed by room temperature HCOOH (formic acid) adsorption [61]. Additional support for the presence of formate species on RuLZ and RuZr catalysts also comes from the characteristic high–frequency vibrational features located at 2962 and 2884 cm^{-1} corresponding to combination bands (O–C–O and C–H deformation) and –C–H stretching modes, respectively [61,62]. Remaining IR bands in Fig. 9b at 1224, 1125, and 1052 cm^{-1} can be assigned to adsorbed carbonates (presumably bidentate carbonates) [63–65]. While RuLa catalyst revealed significantly larger bulk–like carbonate domains, RuLZ and RuZr catalysts showed adsorbed carbonates with a considerably smaller surface coverage. Therefore, relatively higher GDR activity of RuLZ and RuZr catalyst as opposed to that of RuLa can be attributed to smaller extent of coking and differences in the nature of carbonaceous species formed during GDR (*i.e.,* bulk carbonates *vs.* adsorbed carbonates/formates). These findings are in very good agreement with the current TEM and XPS results (Sections 3.2.1 and 3.2.2) and the Thermogravimetric Analysis (TGA) studies (presented in SI section E) revealing significantly larger surface atomic carbon content of the RuLa catalyst after 72 h stability testing as compared to that of RuLZ and RuZr catalysts.

Additional ATR–IR spectroscopic experiments were performed to explain how La^{3+} substitution enhanced the structural integrity and catalytic stability of the RuLZ catalyst as compared to RuZr. Fig. 10 illustrates the ATR–IR spectra of spent RuZr and RuLZ catalysts where the corresponding fresh catalysts were utilized in the acquisition of the relevant background spectra. Vibrational frequency window within 900–400 cm^{-1} revealed the optical phonon vibrations (Zr–O–Zr stretching) of ZrO_2 for monoclinic and tetragonal phases. Spent RuZr catalyst exhibited four distinct negative features located at 765, 680, 562, and 474 cm^{-1}. While the former two frequencies could be ascribed to the Zr–O–Zr phonon vibrations of the monoclinic ZrO_2 phase, the latter two features were associated to the tetragonal zirconia phase [66–69]. Occurrence of the negative features for the RuZr catalyst implied a notable loss in the structural integrity of the zirconia support after 72 h stability test. However, the lack of strong negative vibrational

features for the RuLZ catalyst clearly illustrated its relative stability and enhancement of the catalyst robustness upon stabilization of the zirconia matrix with lantana. This finding is also in alignment with former temperature programmed reduction (TPR) studies reporting that compared to its yttria and lantana stabilized counterparts, pure ZrO_2 was more prone to reducing conditions at elevated temperatures [70, 71].

3.2.5. Elucidation of the electronic and geometric properties of the Ru active sites via CO adsorption and in-situ DRIFTS measurements

Utilization of CO(g) as a probe molecule and its adsorption on RuLZ, RuZr, and RuLa catalyst surfaces revealed several informative vibrational features within 2300 and 1750 cm^{-1} in the *in-situ* DRIFTS experiments which were associated with the formation of various carbonyl species on catalytically active Ru sites. CO adsorption on the fresh RuLZ exhibited two strong vibrational features located at 2061 and 1980 cm^{-1}, as well as relatively weaker signals at 2188, 2117, and 1859 cm^{-1} (Fig. 11a). Based on the experimental findings in literature and the results of DFT calculations on RuO_x dispersed on monoclinic and tetragonal ZrO_2 support materials [72], the major vibrational features at 2061 and 1980 cm^{-1} can be assigned to anti–symmetric and symmetric vibrations of *gem*–dicarbonyl species adsorbed on Ru^{2+} sites (*i.e.* Ru(II) $(CO)_2$), respectively. Alternatively, the bands at 2117 and 2061 cm^{-1} can be attributed to multicarbonyls adsorbed on partially oxidized Ru sites ($Ru^{x+}(CO)_n$), and the band at 1980 cm^{-1} can be assigned to monocarbonyls on partially oxidized Ru ($Ru^{x+}CO$). Furthermore, relatively narrow full width at half maximum (FWHM) of the sharp 2061 cm^{-1} feature is also consistent with the homogeneity of the corresponding Ru^{x+} adsorption sites and possible existence of finely dispersed small Ru clusters on lanthana-stabilized tetragonal zirconia containing support material (Fig. 8a) of the RuLZ catalyst. Mihaylov et al. [73] also extensively studied CO adsorption on Ru/ZrO_2. Presence of the feature located at 2117 cm^{-1} in addition to 2061 and 1980 cm^{-1} features indicated the possible formation of tricarbonyl species on Ru^{3+} (*i.e.* Ru(III) $(CO)_3$) [73]. Note that former studies [74,75] showed that CO can adsorb both in a molecular and a dissociative manner on metallic Ru sites leading to the formation of partially oxidized Ru species. Thus, it is also likely that Ru sites with lower oxidation states (*e.g.*, Ru^0 and $Ru^{\delta+}$) may also be present on the RuLZ catalyst before CO adsorption and these species can be converted to Ru species with higher oxidation states upon CO adsorption and dissociation. Assignments regarding the oxidation state of Ru nanoparticles or Ru clusters with small number of Ru atoms is an ongoing debate in the literature. For instance, it was reported that Ru nanoparticles or Ru clusters with fewer atoms on reducible metal oxide support materials such as ZrO_2 could be found in oxidic states under reducing environments [76]. Even after complete reduction to metallic state, Ru nanoparticles/clusters can be readily oxidized when exposed to air [77]. Furthermore, former DFT calculations suggested that the most stable oxidation state of single atom Ru species on MgO was Ru^{4+}, while associated *in–situ* FTIR spectroscopic analysis also verified the presence of oxidic $Ru^{\delta+}$ single atom Ru species [78].

The last feature located at 2188 cm^{-1} in Fig. 11a can be assigned to CO adsorption on Zr^{4+} and/or on other highly oxidic Ru sites [73,79]. Although it is spectroscopically difficult to identify the exact Ru oxidation state and the coordination nature of the multi–carbonyls [72,73,80,81], it can be argued that Ru exists mostly in the form of Ru and RuO_x on the fresh RuLZ catalyst. Lastly, the weak feature appearing at 1859 cm^{-1} in Fig. 11a corresponds to CO adsorbed on metallic Ru species with a bridging configuration *via* two–fold symmetry.

Exposing the RuLZ catalyst to 72 h stability testing caused visible modifications of the catalyst surface and altered the *in–situ* DRIFTS spectral line shapes as shown in the upper spectrum in Fig. 11a. It was obvious that three features (2117, 2061, and 1980 cm^{-1}) corresponding to multi–carbonyls on oxidized Ru were significantly diminished after 72 h along with the emergence of the strong IR vibration at 2029 cm^{-1}. This new feature was thoroughly discussed in the literature and was attributed to atop (*i.e.,* linear) mono–carbonyl adsorption on reduced (*e. g.,* metallic and/or Ru^{x+}, x < 2) Ru sites [73,80–83]. Observed spectroscopic frequency shifts as well as the decrease in the relative ratio of multi–carbonyls to mono–carbonyls were important spectroscopic implications suggesting the reduction of Ru/RuO_x clusters with H_2, CO, and surface carbon species acting as reducing agents at elevated temperatures during the 72 h GDR reaction. Thus, catalytic deactivation can also be linked to alterations in the oxidation state of the Ru active sites. Increase in *in–situ* DRIFTS signal intensities of the spent RuLZ catalyst as compared to that of the fresh catalyst (Fig. 11a) can be associated to the variations in IR absorption cross-sections of Ru/RuO_x clusters due to reduction RuO_x clusters and alterations in Ru/RuO_x dispersion under reaction conditions.

In–situ DRIFTS analysis was also carried out for the RuZr catalyst
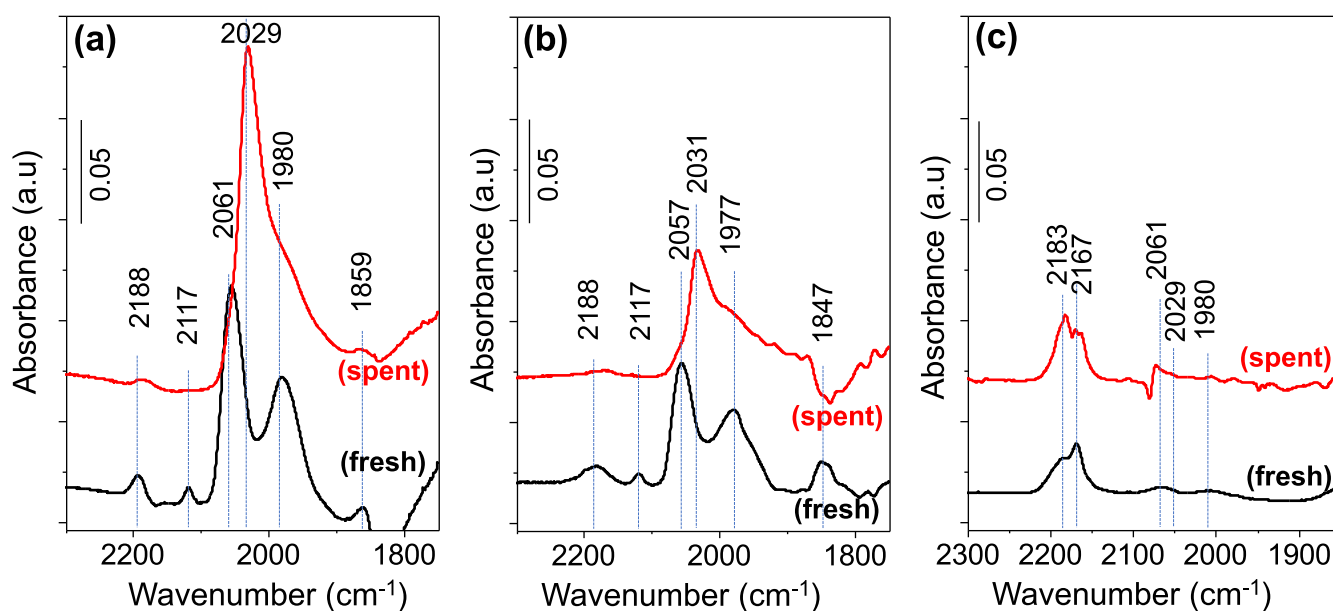
Fig. 11. *In–situ* DRIFTS spectra corresponding to CO adsorption on (a) RuLZ, (b) RuZr and (c) RuLa catalysts in their fresh and spent forms (*i.e.,* after 72 h stability tests at T = 750 °C, CO_2/G = 3, residence time = 3.75 mg_{cat} min/Nml). Spectra were collected under 1.0% CO(g) in Ar(g) at 50 Nml/min flow.

under identical conditions (Fig. 11b) revealing spectroscopic features in close resemblance to that of RuLZ (Fig. 11a). These findings pointed out that the electronic properties of the Ru/RuO_x species on the RuZr catalyst were rather similar to that of the RuLZ. This can be linked to the Zr enriched surfaces of both La_2O_3/ZrO_2 and ZrO_2 supports as evidenced by the current XPS results given in Fig. 7. On the other hand, slightly lower GDR activity of RuZr compared to that of RuLZ can be explained by considering the significantly weaker DRIFTS signal intensities observed for the RuZr catalyst (Fig. 8b) implying that the relative number of exposed Ru active sites on RuZr were smaller due to the lower dispersion of Ru on monoclinic zirconia (note that an identical mass of catalyst, *ca.* 20 mg, was used for all of the measurements given in Fig. 11). This is also consistent with the lower SSA of the RuZr catalyst as compared to that of RuLZ. This result can be due to larger Ru/RuO_x particle size for RuZr catalyst (as predicted by the current TEM data given in Fig. 5a, b) and more likely due to the strong metal support interaction (SMSI) phenomena [50–52], where the reducible zirconia support was spread over the Ru/RuO_x actives sites and covered/blocked these sites rendering them unavailable for the GDR reaction [52,84–87]. This argument can be supported with the fact that ZrO_2 is a relatively more reducible metal oxide as compared to the stabilized $La_2O_3–ZrO_2$ mixed oxide [88] and the current ATR-IR spectroscopic data (Fig. 10) for the spent RuZr catalyst clearly revealed structural deformation of the zirconia support structure after 72 h GDR catalytic stability test. Furthermore, slight decrease in the *in–situ* DRIFTS intensities of the spent RuZr catalyst as compared to that of its fresh counterpart (Fig. 11b) is also consistent with the aging and sintering of the Ru species on the RuZr catalyst after the 72 h stability test or partial covering of Ru species with ZrO_2 support *via* SMSI. Current *in–situ* DRIFTS data given in Fig. 11a, b are also in line with the performance results presented in Fig. 1a suggesting that RuLZ has a better GDR activity than that of RuZr due to the larger number of exposed Ru species both before and after 72 h stability tests.

Fig. 11c shows that the structure of Ru sites on the RuLa catalyst differs significantly from those of RuLZ and RuZr revealing noticeably different DRIFTS line shapes obtained upon CO adsorption. Vibrational features at 2183 and 2167 cm^{-1} in Fig. 11c suggested the presence of highly oxidic Ru^{+x} species ($x \geq 4$) [73] on RuLa as well as CO adsorption on lanthana support, where the oxidation states of Ru species on RuLa were different than those of RuLZ and RuZr. This result pointed out the relationship between the Ru oxidation state and the corresponding GDR activity. As commonly agreed in the literature [16,30,31,47], RWGS shaped up the product distribution in GDR. Existing literature on the mechanism for the CO_2 reduction by H_2 through RWGS typically included two alternative mechanistic routes. These are namely, redox and associative mechanisms, where in both of these mechanistic routes, H_2 dissociation was considered to be one of the key steps [89–91]. Dissociative adsorption of H_2 on Ru takes places *via* electron transfer from the precious metal active site to the antibonding molecular orbital of H_2 and the activation barrier for this electron transfer is dictated by the oxidation state of a noble metal active site [92,93]. Along these lines, it is apparent that highly oxidic and electron deficient Ru species on La_2O_3 as well as the severe coking on RuLa can be considered as the other root causes of its lower catalytic performance. On the other hand, Fig. 11c indicates that Ru oxidation states do not change very significantly after the 72 h stability test, suggesting that RuO_x reduction may not be a prominent cause of deactivation for the RuLa catalyst. Finally, Fig. 11c shows that RuLa reveals the weakest DRIFTS intensities among all other studied catalysts, due to its smallest SSA value, largest average Ru particle size, and the poorest Ru dispersion.

4. Conclusions

Valorization of glycerol, side product of biodiesel synthesis, to syngas *via* its reforming with CO_2 was studied on La_2O_3, ZrO_2 and $La_2O_3–ZrO_2$ supported Ru catalysts. Effects of molar inlet CO_2/G ratio (1–4) and residence time (0.25–3.75 mg_{cat}.min/Nml) on CO_2 conversion, glycerol conversion to gaseous products, and product distribution were studied at 750 °C. Spent catalysts tested under reactive GDR environment were thoroughly characterized to obtain fundamental insights regarding structure/activity/deactivation relationships. Our findings are summarized as follows:

- Catalytic GDR activities of the currently investigated catalysts in 5 h GDR tests carried out at 750 °C, $CO_2/G = 1–4$, and 0.25 mg_{cat} min/Nml increased in the following order: $Ru/La_2O_3 < Ru/ZrO_2 < Ru/La_2O_3–ZrO_2$.
- $Ru/La_2O_3–ZrO_2$ was found to be the best performing and the most stable catalyst among currently investigated catalysts. Strikingly, under similar conditions, performance of $Ru/La_2O_3–ZrO_2$ was on par with the more expensive $Rh/Al_2O_3–ZrO_2–TiO_2$, the best GDR catalyst reported so far in the literature. Stabilization of ZrO_2 with lantana enabled $Ru/La_2O_3–ZrO_2$ to deliver 82% of the pertinent equilibrium CO_2 conversion after the 72 h stability tests. Remarkable performance and stability of $Ru/La_2O_3–ZrO_2$ were attributed to the enhanced structural integrity of the tetragonal zirconia–containing $La_2O_3–ZrO_2$ support material, and its ability to a) gasify most of the surface carbon species during the GDR reaction and prevent coking, b) offer unique Ru oxidation states, c) provide relatively small ($<$ 1 nm) Ru average particle size, d) maintain high Ru dispersion, and e) enable high Ru sintering resistance.
- On both $La_2O_3–ZrO_2$ and ZrO_2, Ru active sites existed as predominantly small clusters with diameters < 1 nm and mostly in Ru^{2+} form with a slight contribution from Ru^{3+} and Ru^0 species. These oxidic Ru species were found to be reduced to metallic and/or Ru^{+x} ($x < 2$) states under reactive GDR conditions, along with minor sintering of Ru particles, particularly in case of RuZr.
- Despite its high initial activity, Ru/ZrO_2 deactivated significantly (by $\sim$33%) at the end of 72 h stability tests due to combined effects of: a) Ru sintering, b) alterations in the monoclinic and tetragonal ZrO_2 crystallographic phases of the support material, c) SMSI between Ru and ZrO_2 resulting in the migration of zirconia over Ru nanoparticles, and d) (to a lesser extent) coking.
- In contrast with its poor 5 h GDR performance, Ru/La_2O_3 was found to be more stable than Ru/ZrO_2 in the first half of the 72 h stability tests. Ru was found to be in a highly oxidic form (*i.e.*, Ru^{+x} species, $x \geq 4$) on RuLa and the oxidation state of Ru nanoparticles on La_2O_3 remained relatively unchanged during stability tests. Significant loss in catalytic activity of Ru/La_2O_3 catalysts at the end of stability test was attributed predominantly to a) severe coking, and b) crystallographic deformation of support material involving dehydroxylation and carbonation of lanthana.

CRediT authorship contribution statement

Mert Ozden: Methodology, Validation, Formal analysis, Investigation, Writing – original draft, Visualization. **Zafer Say:** Methodology, Validation, Formal analysis, Investigation, Writing – original draft, Writing – review & editing, Visualization. **Yusuf Kocak:** Formal analysis, Investigation, Writing – original draft, Visualization. **Kerem Emre Ercan:** Formal analysis, Investigation, Visualization. **Ahsan Jalal:** Formal analysis, Investigation, Visualization. **Emrah Ozensoy:** Conceptualization, Methodology, Writing – original draft, Writing – review & editing, Supervision, Project administration, Funding acquisition. **Ahmet K. Avci:** Conceptualization, Methodology, Writing – original draft, Writing – review & editing, Supervision, Project administration, Funding acquisition.

Declaration of Competing Interest

The authors declare that they have no known competing financial interests or personal relationships that could have appeared to influence

the work reported in this paper.

Acknowledgments

Appendix A. Supporting information

Supplementary data associated with this article can be found in the online version at doi:10.1016/j.apcata.2022.118577.

References

[1] J.V. Gerpen, Fuel Process. Technol. 86 (10) (2005) 1097–1107, https://doi.org/10.1016/j.fuproc.2004.11.005.

[2] R.L. Naylor, M.M. Higgins, Renew. Sustain. Energy Rev. 77 (2017) 695–705, https://doi.org/10.1016/j.rser.2017.04.026.

[3] M.R. Monteiro, C.L. Kugelmeier, R.S. Pinheiro, M.O. Batalha, A. da Silva César, Renew. Sustain. Energy Rev. 88 (2018) 109–122, https://doi.org/10.1016/j.rser.2018.02.019.

[4] C.A. Schwengber, H.J. Alves, R.A. Schaffner, F.A. da Silva, R. Sequinel, V.R. Bach, R.J. Ferracin, Renew. Sustain. Energy Rev. 58 (2016) 259–266, https://doi.org/10.1016/j.rser.2015.12.279.

[5] R. Ciriminna, C.D. Pina, M. Rossi, M. Pagliaro, Eur. J. Lipid Sci. Technol. 116 (10) (2014) 1432–1439, https://doi.org/10.1002/ejlt.201400229.

[6] Y.-C. Lin, Int. J. Hydrog. Energy 38 (6) (2013) 2678–2700, https://doi.org/10.1016/j.ijhydene.2012.12.079.

[7] J.M. Silva, M.A. Soria, L.M. Madeira, Renew. Sustain. Energy Rev. 42 (2015) 1187–1213, https://doi.org/10.1016/j.rser.2014.10.084.

[8] N.D. Charisiou, K. Polychronopoulou, A. Asif, M.A. Goula, Surf. Coat. Technol. 352 (2018) 92–111, https://doi.org/10.1016/j.surfcoat.2018.08.008.

[9] D. Pakhare, J. Spivey, Chem. Soc. Rev. 43 (22) (2014) 7813–7837, https://doi.org/10.1039/C3CS60395D.

[10] C. Agrafiotis, H. von Storch, M. Roeb, C. Sattler, Renew. Sustain. Energy Rev. 29 (2014) 656–682, https://doi.org/10.1016/j.rser.2013.08.050.

[11] A.C.D. Freitas, R. Guirardello, Int. J. Hydrog. Energy 39 (31) (2014) 17969–17984, https://doi.org/10.1016/j.ijhydene.2014.03.130.

[12] T. Valliyappan, N.N. Bakhshi, A.K. Dalai, Bioresour. Technol. 99 (10) (2008) 4476–4483, https://doi.org/10.1016/j.biortech.2007.08.069.

[13] D.L. Trimm, Catal. Today 49 (1–3) (1999) 3–10, https://doi.org/10.1016/s0920-5861(98)00401-5.

[14] J.R. Rostrup-Nielsen, Catalytic steam reforming, in: J.R. Anderson, M. Boudart (Eds.), Catalysis – Science and Technology, Springer-Verlag, Berlin, 1984, pp. 1–117.

[15] J.R. Rostrup-Nielsen, Catal. Today 63 (2–4) (2000) 159–164, https://doi.org/10.1016/s0920-5861(00)00455-7.

[16] S. Bac, S. Keskin, A.K. Avci, Sustain. Energy Fuels 4 (3) (2020) 1029–1047, https://doi.org/10.1039/C9SE00967A.

[17] Y.T. Shah, T.H. Gardner, Cat. Rev. Sci. Eng. 56 (4) (2014) 476–536, https://doi.org/10.1080/01614940.2014.946848.

[18] S. Bac, S. Keskin, A.K. Avci, Int. J. Hydrog. Energy 45 (2020) 34888–34917, https://doi.org/10.1016/j.ijhydene.2019.11.237.

[19] M. Tavanarad, F. Meshkani, M. Rezaei, J. CO2 Util. 24 (2018) 298–305, https://doi.org/10.1016/j.jcou.2018.01.009.

[20] N.N. Mohd Arif, S.Z. Abidin, O.U. Osazuwa, D.-V.N. Vo, M.T. Azizan, Y.H. Taufiq-Yap, Int. J. Hydrog. Energy 44 (2019) 20857–20871, https://doi.org/10.1016/j.ijhydene.2018.06.084.

[21] N.A. Roslan, N.N. Mohd Arif, J.L. Jaspin, N.A. Mohamed Razali, S. Zainal Abidin, Energy Sources A Recovery Util. Environ. Eff. (2019) 1–13, https://doi.org/10.1080/15567036.2019.1645762.

[22] H.C. Lee, K.W. Siew, J. Gimbun, C.K. Cheng, Chem. Eng. J. 255 (2014) 245–256, https://doi.org/10.1016/j.cej.2014.06.044.

[23] H.C. Lee, K.W. Siew, M.R. Khan, S.Y. Chin, J. Gimbun, C.K. Cheng, J. Energy Chem. 23 (5) (2014) 645–656, https://doi.org/10.1016/S2095-4956(14)60196-0.

[24] A. Dehghanpoor-Gharashah, M. Rezaei, F. Meshkani, Int. J. Hydrog. Energy 46 (43) (2021) 22454–22462, https://doi.org/10.1016/j.ijhydene.2021.04.072.

[25] K.W. Siew, H.C. Lee, J. Gimbun, S.Y. Chin, M.R. Khan, Y.H. Taufiq-Yap, C. K. Cheng, Renew. Energy 74 (2015) 441–447, https://doi.org/10.1016/j.renene.2014.08.048.

[26] K.W. Siew, H.C. Lee, M.R. Khan, J. Gimbun, C.K. Cheng, J. Energy Chem. 24 (3) (2015) 366–373, https://doi.org/10.1016/S2095-4956(15)60324-2.

[27] K.W. Siew, H.C. Lee, J. Gimbun, C.K. Cheng, J. Energy Chem. 23 (1) (2014) 15–21, https://doi.org/10.1016/S2095-4956(14)60112-1.

[28] N. Harun, S.Z. Abidin, O.U. Osazuwa, Y.H. Taufiq-Yap, M.T. Azizan, Int. J. Hydrog. Energy 44 (1) (2019) 213–225, https://doi.org/10.1016/j.ijhydene.2018.03.093.

[29] N. Harun, J. Gimbun, M.T. Azizan, S.Z. Abidin, Bull. Chem. React. Eng. Catal. 11 (2) (2016) 220–229.

[30] P.S. Bulutoglu, Z. Say, S. Bac, E. Ozensoy, A.K. Avci, Appl. Catal. A 564 (2018) 157–171, https://doi.org/10.1016/j.apcata.2018.07.027.

[31] S. Bac, Z. Say, Y. Kocak, K.E. Ercan, M. Harfouche, E. Ozensoy, A.K. Avci, Appl. Catal. B 256 (2019), 117808, https://doi.org/10.1016/j.apcatb.2019.117808.

[32] M. Tavanarad, F. Meshkani, M. Rezaei, Catal. Lett. 148 (1) (2018) 164–172, https://doi.org/10.1007/s10562-017-2221-3.

[33] Johnson Matthey Plc. 〈http://www.platinum.matthey.com/prices/price-charts〉. (Accessed 1 October 2021.

[34] J.R. Rostrup-Nielsen, J.H.B. Hansen, J. Catal. 144 (1) (1993) 38–49, https://doi.org/10.1006/jcat.1993.1312.

[35] A.N.J. van Keulen, K. Seshan, J.H.B.J. Hoebink, J.R.H. Ross, J. Catal. 166 (2) (1997) 306–314, https://doi.org/10.1006/jcat.1997.1539.

[36] S. Therdthianwong, C. Siangchin, A. Therdthianwong, Fuel Process. Technol. 89 (2) (2008) 160–168, https://doi.org/10.1016/j.fuproc.2007.09.003.

[37] M.C.J. Bradford, M.A. Vannice, J. Catal. 173 (1) (1998) 157–171, https://doi.org/10.1006/jcat.1997.1910.

[38] H.S. Whang, M.S. Choi, J. Lim, C. Kim, I. Heo, T.-S. Chang, H. Lee, Catal. Today 293–294 (2017) 122–128, https://doi.org/10.1016/j.cattod.2016.12.034.

[39] M.A. Goula, N.D. Charisiou, G. Siakavelas, L. Tzounis, I. Tsiaoussis, P. Panagiotopoulou, G. Goula, I.V. Yentekakis, Int. J. Hydrog. Energy 42 (19) (2017) 13724–13740, https://doi.org/10.1016/j.ijhydene.2016.11.196.

[40] X. Bai, G. Xie, Y. Guo, L. Tian, H.M. El-Hosainy, A.E. Awadallah, S. Ji, Z.-j. Wang, Catal. Today 368 (2021) 78–85, https://doi.org/10.1016/j.cattod.2019.12.033.

[41] Y. Guo, J. Zou, X. Shi, P. Rukundo, Z.-j. Wang, ACS Sustain. Chem. Eng. 5 (3) (2017) 2330–2338, https://doi.org/10.1021/acssuschemeng.6b02661.

[42] Y. Guo, Y. Li, Y. Ning, Q. Liu, L. Tian, R. Zhang, Q. Fu, Z.-j Wang, Ind. Eng. Chem. Res. 59 (35) (2020) 15506–15514, https://doi.org/10.1021/acs.iecr.0c02444.

[43] J. Sun, S. Wang, Y. Guo, M. Li, H. Zou, Z.-j Wang, Catal. Commun. 104 (2018) 53–56, https://doi.org/https://doi.org/10.1016/j.catcom.2017.10.021.

[44] S. Wen, M. Liang, J. Zou, S. Wang, X. Zhu, L. Liu, Z.-j Wang, J. Mater. Chem. A 3 (25) (2015) 13299–13307, https://doi.org/10.1039/C5TA01699A.

[45] Z.I. Onsan, A.K. Avci, Reactor design for fuel processing, in: D. Shekhawat, J. J. Spivey, D.A. Berry (Eds.), Fuel Cells: Technologies for Fuel Processing, Elsevier Science, Amsterdam, 2011, pp. 451–516, https://doi.org/10.1016/b978-0-444-53563-4.10014-8.

[46] J. Yu, J.A. Odriozola, T.R. Reina, Catalysts 9 (12) (2019) 1015, https://doi.org/10.3390/catal9121015.

[47] A.C.D. Freitas, R. Guirardello, Int. J. Hydrog. Energy 39 (31) (2014) 17969–17984, https://doi.org/10.1016/j.ijhydene.2014.03.130.

[48] J. Jones, H. Xiong, A.T. DeLaRiva, E.J. Peterson, H. Pham, S.R. Challa, G. Qi, S. Oh, M.H. Wiebenga, X.I. Pereira Hernández, Y. Wang, A.K. Datye, Science 353 (6295) (2016) 150, https://doi.org/10.1126/science.aaf8800.

[49] T.W. Hansen, A.T. DeLaRiva, S.R. Challa, A.K. Datye, Acc. Chem. Res. 46 (8) (2013) 1720–1730, https://doi.org/10.1021/ar3002427.

[50] D.W. Goodman, Chem. Rev. 95 (3) (1995) 523–536, https://doi.org/10.1021/cr00035a004.

[51] M. Haruta, CATTECH 6 (3) (2002) 102–115, https://doi.org/10.1023/A:1020181423055.

[52] C.T. Campbell, Nat. Chem. 4 (8) (2012) 597–598, https://doi.org/10.1038/nchem.1412.

[53] J.D. Rodriguez-Blanco, S. Shaw, L.G. Benning, Nanoscale 3 (1) (2011) 265–271, https://doi.org/10.1039/C0NR00589D.

[54] F.A. Andersen, L. Brečević, Acta Chem. Scand. 45 (1991) 1018–1024.

[55] M. Farhadi Khouzani, D.M. Chevrier, P. Güttlein, K. Hauser, P. Zhang, N. Hedin, D. Gebauer, CrystEngComm 17 (26) (2015) 4842–4849, https://doi.org/10.1039/C5CE00720H.

[56] X.E. Verykios, Energy 28 (10) (2003) 1045–1063, https://doi.org/10.1016/S0360-3199(02)00215-X.

[57] S. Irusta, L.M. Cornaglia, E.A. Lombardo, Mater. Chem. Phys. 86 (2) (2004) 440–447, https://doi.org/10.1016/j.matchemphys.2004.04.017.

[58] T. Levan, M. Che, J.M. Tatibouet, M. Kermarec, J. Catal. 142 (1) (1993) 18–26, https://doi.org/10.1006/jcat.1993.1185.

[59] A. Demény, P. Németh, G. Czuppon, S. Leél-Őssy, M. Szabó, K. Judik, T. Németh, J. Stieber, Sci. Rep. 6 (1) (2016) 39602, https://doi.org/10.1038/srep39602.

[60] M.A. Henderson, S.D. Worley, J. Phys. Chem. 89 (8) (1985) 1417–1423, https://doi.org/10.1021/j100254a023.

[61] M.R. Prairie, A. Renken, J.G. Highfield, K. Ravindranathan Thampi, M. Grätzel, J. Catal. 129 (1) (1991) 130–144, https://doi.org/10.1016/0021-9517(91)90017-X.

[62] F. Solymosi, A. Erdöhelyi, M. Kocsis, J. Chem. Soc. Faraday Trans. 77 (5) (1981) 1003–1012, https://doi.org/10.1039/F19817701003.

[63] E. Gallei, G. Stumpf, J. Colloid Interface Sci. 55 (2) (1976) 415–420, https://doi.org/10.1016/0021-9797(76)90051-5.

[64] A. Westermann, B. Azambre, M.C. Bacariza, I. Graça, M.F. Ribeiro, J.M. Lopes, C. Henriques, Appl. Catal. B (174–175) (2015) 120–125, https://doi.org/10.1016/j.apcatb.2015.02.026.

[65] P. Osorio-Vargas, C.H. Campos, R.M. Navarro, J.L.G. Fierro, P. Reyes, Appl. Catal. A 505 (2015) 159–172, https://doi.org/10.1016/j.apcata.2015.07.037.

[66] S. Jayakumar, P.V. Ananthapadmanabhan, K. Perumal, T.K. Thiyagarajan, S. C. Mishra, L.T. Su, A.I.Y. Tok, J. Guo, Mater. Sci. Eng. B 176 (12) (2011) 894–899, https://doi.org/10.1016/j.mseb.2011.05.013.

[67] A. Feinberg, C.H. Perry, J. Phys. Chem. Solids 42 (6) (1981) 513–518, https://doi.org/10.1016/0022-3697(81)90032-9.

[68] J. Chandradass, M. Balasubramanian, K. Hyeon Kim, J. Exp. Nanosci. 6 (1) (2011) 38–48, https://doi.org/10.1080/17458081003762813.

[69] S. Chen, Y. Yin, D. Wang, Y. Liu, X. Wang, J. Cryst. Growth 282 (3) (2005) 498–505, https://doi.org/10.1016/j.jcrysgro.2005.05.017.

[70] M. Kogler, E.-M. Köck, T. Bielz, K. Pfaller, B. Klötzer, D. Schmidmair, L. Perfler, S. Penner, J. Phys. Chem. C 118 (16) (2014) 8435–8444, https://doi.org/10.1021/jp5008472.

[71] S.H. Park, B.H. Chun, S.H. Kim, Korean J. Chem. Eng. 28 (2011) 402–408.

[72] H.V. Thang, S. Tosoni, L. Fang, P. Bruijnincx, G. Pacchioni, ChemCatChem 10 (12) (2018) 2634–2645, https://doi.org/10.1002/cctc.201800246.

[73] M. Mihaylov, O. Lagunov, E. Ivanova, K. Hadjiivanov, J. Phys. Chem. C. 115 (28) (2011) 13860–13867, https://doi.org/10.1021/jp203944c.

[74] E. Guglielminotti, F. Boccuzzi, M. Manzoli, F. Pinna, M. Scarpa, J. Catal. 192 (1) (2000) 149–157, https://doi.org/10.1006/jcat.2000.2835.

[75] K. Hadjiivanov, J.C. Lavalley, J. Lamotte, F. Maugé, J. Saint-Just, M. Che, J. Catal. 176 (2) (1998) 415–425, https://doi.org/10.1006/jcat.1998.2038.

[76] T. Komanoya, T. Kinemura, Y. Kita, K. Kamata, M. Hara, J. Am. Chem. Soc. 139 (33) (2017) 11493–11499, https://doi.org/10.1021/jacs.7b04481.

[77] F. Su, L. Lv, F.Y. Lee, T. Liu, A.I. Cooper, X.S. Zhao, J. Am. Chem. Soc. 129 (46) (2007) 14213–14223, https://doi.org/10.1021/ja072697v.

[78] B.B. Sarma, P.N. Plessow, G. Agostini, P. Concepción, N. Pfänder, L. Kang, F. R. Wang, F. Studt, G. Prieto, J. Am. Chem. Soc. 142 (35) (2020) 14890–14902, https://doi.org/10.1021/jacs.0c03627.

[79] E. Guglielminotti, F. Boccuzzi, M. Manzoli, F. Pinna, M. Scarpa, J. Catal. 192 (1) (2000) 149–157, https://doi.org/10.1006/jcat.2000.2835.

[80] S.Y. Chin, C.T. Williams, M.D. Amiridis, J. Phys. Chem. B 110 (2) (2006) 871–882, https://doi.org/10.1021/jp053908q.

[81] K. Hadjiivanov, J.C. Lavalley, J. Lamotte, F. Maugé, J. Saint-Just, M. Che, J. Catal. 176 (2) (1998) 415–425, https://doi.org/10.1006/jcat.1998.2038.

[82] K.L. Kostov, H. Rauscher, D. Menzel, Surf. Sci. 278 (1) (1992) 62–86, https://doi.org/10.1016/0039-6028(92)90584-S.

[83] F. Gao, D.W. Goodman, Phys. Chem. Chem. Phys. 14 (19) (2012) 6688–6697, https://doi.org/10.1039/C2CP40121E.

[84] S.J. Tauster, Acc. Chem. Res. 20 (11) (1987) 389–394, https://doi.org/10.1021/ar00143a001.

[85] J. Ftouni, A. Muñoz-Murillo, A. Goryachev, J.P. Hofmann, E.J.M. Hensen, L. Lu, C. J. Kiely, P.C.A. Bruijnincx, B.M. Weckhuysen, ACS Catal. 6 (8) (2016) 5462–5472, https://doi.org/10.1021/acscatal.6b00730.

[86] A. Beck, X. Huang, L. Artiglia, M. Zabilskiy, X. Wang, P. Rzepka, D. Palagin, M.-G. Willinger, J.A. van Bokhoven, Nat. Commun. 11 (1) (2020) 3220, https://doi.org/10.1038/s41467-020-17070-2.

[87] S. Zhang, P.N. Plessow, J.J. Willis, S. Dai, M. Xu, G.W. Graham, M. Cargnello, F. Abild-Pedersen, X. Pan, Nano Lett. 16 (7) (2016) 4528–4534, https://doi.org/10.1021/acs.nanolett.6b01769.

[88] M.V. Ganduglia-Pirovano, A. Hofmann, J. Sauer, Surf. Sci. Rep. 62 (6) (2007) 219–270, https://doi.org/10.1016/j.surfrep.2007.03.002.

[89] S.-I. Fujita, M. Usui, N. Takezawa, J. Catal. 134 (1) (1992) 220–225, https://doi.org/10.1016/0021-9517(92)90223-5.

[90] M.J.L. Ginés, A.J. Marchi, C.R. Apesteguía, Appl. Catal. A 154 (1) (1997) 155–171, https://doi.org/10.1016/S0926-860X(96)00369-9.

[91] S. Roy, A. Cherevotan, S.C. Peter, ACS Energy Lett. 3 (8) (2018) 1938–1966, https://doi.org/10.1021/acsenergylett.8b00740.

[92] W.C. Conner, J.L. Falconer, Chem. Rev. 95 (3) (1995) 759–788, https://doi.org/10.1021/cr00035a014.

[93] G. Righi, R. Magri, A. Selloni, J. Phys. Chem. C 123 (15) (2019) 9875–9883, https://doi.org/10.1021/acs.jpcc.9b00609.